IOP Publishing Journal of Physics B: Atomic, Molecular and Optical Physics
J. Phys. B: At. Mol. Opt. Phys. **53** (2020) 075002 (19pp) https://doi.org/10.1088/1361-6455/ab69a7

Relativistic impulse approximation in Compton scattering

Chen-Kai Qiao[1], Hsin-Chang Chi[2], Lei Zhang[1], Peng Gu[1], Cheng-Pang Liu[2], Chang-Jian Tang[1], Shin-Ted Lin[1,5] and Keh-Ning Huang[3,4,5]

[1] College of Physics, Sichuan University, Chengdu, Sichuan, 610064, People's Republic of China
[2] Department of Physics, National Dong Hwa University, Shoufeng, Hualien, 97401, People's Republic of China
[3] Institute of Atomic and Molecular Physics, Sichuan University, Chengdu, Sichuan, 610064, People's Republic of China
[4] Department of Physics, National Taiwan University, Taipei, 10617, People's Republic of China

E-mail: stlin@scu.edu.cn and knhuang1206@gmail.com

Received 7 June 2019, revised 23 December 2019
Accepted for publication 9 January 2020
Published 5 March 2020

Abstract

Relativistic impulse approximation (RIA) has been widely used in atomic, condensed matter, nuclear, and elementary particle physics. In former treatments of RIA formulation, differential cross sections for Compton scattering processes were factorized into atomic Compton profiles by performing further simplified approximations in the integration. In this study, we develop an 'exact' numerical method without using any further simplified approximations or factorization treatments. The validity of the approximations and factorizations used in former RIA treatments can be tested using our approach. Calculations for C, Cu, Ge, and Xe atomic systems are carried out using Dirac–Fock (DF) wavefunctions, and comparisons between the proposed approach and former treatments of RIA are performed and discussed in detail. Numerical results indicate that these simplified approximations work reasonably in the Compton peak region, and our results have little difference with the best of the former RIA treatments in the entire energy region. Meanwhile, in regions far from the Compton peak, the RIA results become inaccurate, even when our 'exact' numerical treatment is used.

Keywords: Compton scattering, relativistic impulse approximation, differential cross section, Compton profile, Dirac–Fock theory

(Some figures may appear in colour only in the online journal)

1. Introduction

Atomic Compton scatterings, which have been widely investigated over the past few decades, are expressed as follows:

$$\hbar\omega_i + A \longrightarrow \hbar\omega_f + e^- + A^+ \tag{1}$$

.Many aspects of physics, such as electron correlations [1, 2], electron momentum distributions [3–5], Fermi surfaces [6], x-ray, and gamma-ray radiations [7–9], have been revealed through them. Moreover, Compton scatterings have been utilized to develop the modern gamma-ray spectrometer and imaging devices [10–12].

For convenience, Compton scattering is conventionally approached using the Klein–Nishina formula from free electron approximation (FEA) [13, 14]. In FEA, electron interactions with atomic ions are neglected, and electrons are also assumed to be at rest prior to photon scatterings in the laboratory frame. In the Klein–Nishina formula, the energy of the scattered photon ω_C is completely determined using its scattering angle θ as follows:

$$\omega_C = \frac{\omega_i}{1 + \omega_i(1 - \cos\theta)/mc^2}. \tag{2}$$

The Klein–Nishina formula works perfectly in high-energy regions, where the electrons are asymptotically free. However, in low-energy regions, where the atomic binding effects

[5] Authors to whom any correspondence should be addressed.

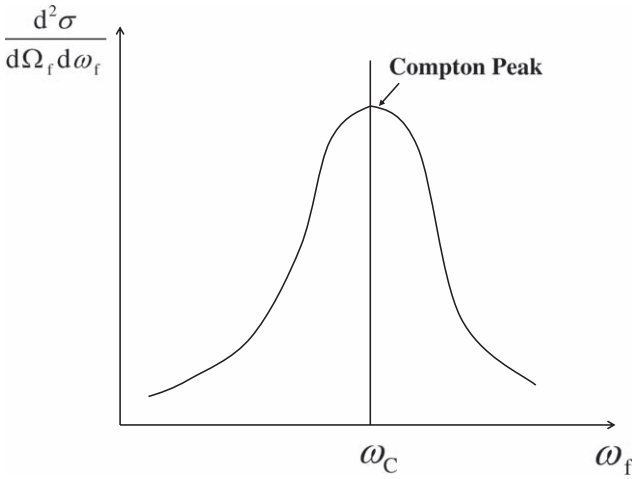

Figure 1. Compton spectrum in the IA model at the scattering angle θ.

are present, the FEA becomes inappropriate and the Klein–Nishina formula fails to explain the experiments [7].

The atomic binding effects are systematically treated in impulse approximation (IA) [15–20], in which the electrons in an atom have a momentum distribution. The motion of electrons causes a Doppler broadened Compton spectrum, as shown in figure 1. In the former treatments of IA models, the doubly-differential cross section (DDCS) of Compton scatterings can be factorized into two parts, given by

$$\left(\frac{d^2\sigma}{d\omega_f d\Omega_f}\right)_{IA} = Y \cdot J. \tag{3}$$

Here, Y is a factor dependent on kinematical and dynamical properties of Compton scatterings, and irrelevant to the electronic structure of target materials. The correction factor J, known as the Compton profile, is related to the momentum distributions of electrons in the atomic or molecular ground state.

Currently, former IA treatments, which incorporate the factorization in equation (3), are widely applied in interdisciplinary studies, particularly in condensed matter, nuclear, and elementary particle physics. Sophisticated electronic structures [21, 22], electron correlations [1, 2], band structures, and Fermi surfaces [6, 23] in condensed matter physics are studied using Compton profiles. The current Geant4 and other Monte Carlo simulation packages in nuclear and particle physics adopt the IA formulation and Compton profiles [24–26]. The conclusions of these interdisciplinary studies depend strictly on the validity of factorization in equation (3). Previously, it was believed that this factorization result adopted in former relativistic impulse approximation (RIA) treatments does not essentially change the physical results [17]. However, this assumption has not been quantitatively analyzed in recent years. Thus, this study is focused on clarifying whether essential differences in IA formulations exist with and without these factorization treatments.

Therefore, for a comprehensive study of atomic Compton scattering processes, in this study we develop an 'exact' numerical treatment of RIA without invoking the factorization in equation (3). Then we apply the present approach to Compton scattering with several atomic systems, and the results are compared with those of former treatments of RIA. Furthermore, a careful analysis of the adequacy of former RIA treatments and the validity of factorization in equation (3) is provided in this work. Moreover, effective Compton profiles (ECPs) are proposed and analyzed to quantify the differences between our results and those of former RIA treatments.

Recently, LaJohn compared various treatments of RIA formulation in a similar manner, and achieved the nonrelativistic limit of RIA for low-momentum-transfer cases [27]. However, his work is limited to hydrogen-like systems. In our study, more complicated atomic systems are considered. We apply the present scheme to the atoms C, Cu, Ge, and Xe, which are chosen to represent elements in the small-Z, middle-Z, and large-Z regimes. To obtain the ground state wavefunctions for atomic systems, we have employed the fully relativistic Dirac–Fock (DF) theory [28–32]. In the DF formalism, electrons in atomic systems are quantized and many-body effects, including electron exchange and electron correlation interactions, are effectively considered.

Recently, there has been great interest in experimentally detecting dark matter particles [33–39] and neutrino-less double beta decays [40–44]. These experiments, which utilize high-purity germanium and xenon detectors, require a sufficiently low radiation background. Compton scattering is one of the most dominant radiation backgrounds for x-ray and gamma rays which must be suppressed and subtracted. Therefore, studying the atomic Compton scattering effects in detectors could have a great impact on these elementary particle experiments. Recent studies using former treatments of RIA have indicated that low-momentum transfer Compton scattering plays a remarkable role in dark matter direct detections [45, 46]. Further, our method can be easily applied to this area, and could impact and guide the analysis and subtraction of Compton scattering backgrounds in particle physics experiments.

This paper is organized as follows: section 2 introduces the RIA formulation, and is divided into two subsections. In section 2.1, we briefly review the former treatments of Compton scattering in RIA formulation. In section 2.2, we describe our present numerical treatment of RIA for application to atomic Compton scatterings. The results and comparisons of our approach and former RIA treatments are presented in section 3. Finally, the conclusions and future perspectives are provided in section 4.

2. RIA

2.1. Former treatments

In this section, we give a theoretical description of the former treatments of RIA formulations for Compton scatterings. The nonrelativistic-IA approach can be derived similar to the relativistic case.

In the RIA formulations, consider an incident photon with energy ω_i and momentum $\boldsymbol{k}_i$ scattering with an electron which has energy E_i and momentum $\boldsymbol{p}_i$. After scattering, the

energy and momentum of the emitted photon are ω_f and $\boldsymbol{k}_f$, and the energy and momentum of the final state electron are E_f and $\boldsymbol{p}_f$. Then the DDCS of Compton scattering in the RIA formulation is given by [17–19]

$$\frac{d^2\sigma}{d\omega_f d\Omega_f} = \frac{r_0^2 m^2 c^4}{2}\frac{\omega_f}{\omega_i} \times \int d^3p_i \rho(\boldsymbol{p}_i)\frac{X(K_i, K_f)}{E_i E_f}\delta(E_i + \omega_i - E_f - \omega_f) \tag{4}$$

where r_0 is the electron classical charge radius, functions K_i, K_f are defined as

$$K_i = k_i^\mu \cdot p_{i\mu} = \frac{E_i \cdot \omega_i}{c^2} - \boldsymbol{p}_i \cdot \boldsymbol{k}_i \tag{5}$$

$$K_f = k_f^\mu \cdot p_{i\mu} = \frac{E_i \cdot \omega_f}{c^2} - \boldsymbol{p}_i \cdot \boldsymbol{k}_f = K_i - \frac{\omega_i \omega_f (1 - \cos\theta)}{c^2} \tag{6}$$

and the kernel function $X(K_i, K_f)$ is defined as

$$X(K_i, K_f) = \frac{K_i}{K_f} + \frac{K_f}{K_i} + 2m^2c^2\left(\frac{1}{K_i} - \frac{1}{K_f}\right) + m^4c^4\left(\frac{1}{K_i} - \frac{1}{K_f}\right)^2. \tag{7}$$

Here, $\rho(\boldsymbol{p}_i)$ denotes the momentum distribution of electrons, which is calculated through

$$\rho(\boldsymbol{p}_i) = \sum_a |\phi_a(\boldsymbol{p}_i)|^2. \tag{8}$$

Here, the sum is over all electrons, and $\phi_a(\boldsymbol{p}_i)$ is the momentum wavefunction for the a-th electron, which is related to the electron's position wavefunction $\psi_a(\boldsymbol{r})$ through Fourier transformation

$$\phi_a(\boldsymbol{p}_i) = \frac{1}{(2\pi)^{3/2}}\int d^3r \psi_a(\boldsymbol{r}) e^{i\boldsymbol{p}_i \cdot \boldsymbol{r}}. \tag{9}$$

In this work, we employ the fully relativistic DF theory to calculate the total wavefunctions for atomic ground states and the wavefunctions for individual electrons.

The integration in (4) is over all components of $\boldsymbol{p}_i$, namely p_x, p_y, p_z, respectively. However, when one of these components, such as p_z, is integrated out, the Dirac delta function $\delta(E_i + \omega_i - E_f - \omega_f)$ in the integrand constrains the p_z component to be a fixed value, leaving p_x and p_y components in the integral. Further, the fixed value for the p_z component can be completely determined by energy and momentum conservations. For convenience, we can introduce a coordinate system xyz such that the z axis represents the momentum transfer direction. In this coordinate system, the p_z component can be expressed as:

$$p_z = -\frac{\boldsymbol{p}_i \cdot \boldsymbol{q}}{q} = \frac{\omega_i\omega_f(1 - \cos\theta) - E(p_z)(\omega_i - \omega_f)}{c^2 q} \tag{10}$$

where $E(p_z) = \sqrt{m^2c^4 + p_z^2c^2}$ and q is the modulus of the momentum transfer vector $\boldsymbol{q} \equiv \boldsymbol{k}_i - \boldsymbol{k}_f$. Furthermore, a previous study revealed that p_z and $E(p_z)$ are exactly the energy and momentum minimum of the initial state electrons activated in Compton scattering [27], namely

$$p_i^{\min} = |p_z|; \quad E_i^{\min} = E(p_z). \tag{11}$$

In many literatures [19, 20, 24, 25, 47], a convenient approximation for the p_z component is proposed as follows

$$p_z \approx \frac{\omega_i\omega_f(1 - \cos\theta) - mc^2(\omega_i - \omega_f)}{c^2 q}. \tag{12}$$

This approximation works well in small p_z regions, however, it can cause notable discrepancies in large p_z regions. The coordinate system xyz is illustrated in figure 2.

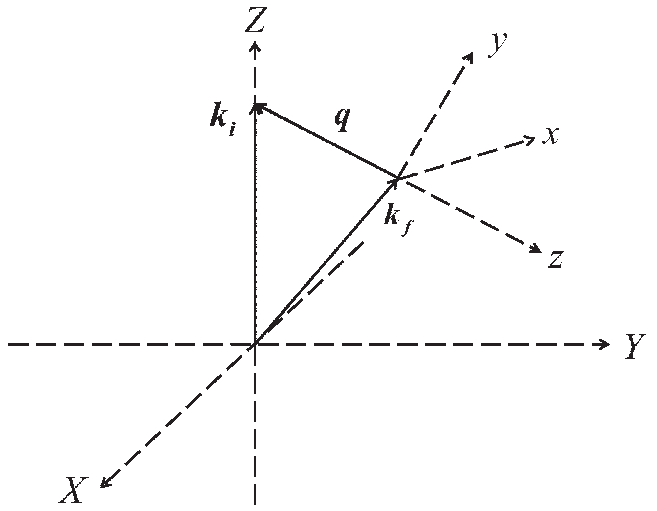

Figure 2. Coordinate systems XYZ and xyz. Coordinate system XYZ is chosen such that the Z axis is along the direction of initial photon $\boldsymbol{k}_i$, and the X axis can be chosen as an arbitrary direction perpendicular to the Z axis. The direction of the scattered photon is denoted as $\boldsymbol{k}_f$, and the vector $\boldsymbol{q}$ is defined as $\boldsymbol{q} \equiv \boldsymbol{k}_i - \boldsymbol{k}_f$. The z axis represents the momentum transfer direction.

In previous studies, Ribberfors *et al* found that the kernel function $X(K_i, K_f)$ in equation (4) is a slow-varying function and therefore can be pulled out of the integration [17, 19, 20]. Successively, this kernel is furthermore approximated by

$$X(K_i, K_f) \approx \overline{X}(p_z) = \frac{K_i(p_z)}{K_f(p_z)} + \frac{K_f(p_z)}{K_i(p_z)} + 2m^2c^2 \times \left(\frac{1}{K_i(p_z)} - \frac{1}{K_f(p_z)}\right) + m^4c^4\left(\frac{1}{K_i(p_z)} - \frac{1}{K_f(p_z)}\right)^2 \tag{13}$$

where

$$K_i(p_z) = \frac{\omega_i E(p_z)}{c^2} + \frac{\omega_i(\omega_i - \omega_f\cos\theta)p_z}{c^2 q} \tag{14}$$

$$K_f(p_z) = K_i(p_z) - \frac{\omega_i\omega_f(1 - \cos\theta)}{c^2}. \tag{15}$$

Using the above assumptions, the DDCS of Compton scatterings in the former RIA treatments is given by

$$\left(\frac{d^2\sigma}{d\omega_f d\Omega_f}\right)_{RIA} = \frac{r_0^2}{2}\frac{m}{q}\frac{mc^2}{E(p_z)}\frac{\omega_f}{\omega_i}\overline{X}(p_z)J(p_z) = \overline{Y}^{RIA}\cdot J(p_z) \quad (16)$$

where $J(p_z)$ is an integral for p_x and p_y components. The same results can be derived from equation (4) through integration by part [17].

An alternative and simpler approximation of the kernel function $X(K_i, K_f)$ can be made by taking the $p_z \to 0$ limit of $\overline{X}(p_z)$, which finally gives its Klein–Nishina value [19, 20]

$$X(K_i, K_f) \approx X_{KN} = \frac{\omega_i}{\omega_f} + \frac{\omega_f}{\omega_i} - \sin^2\theta. \quad (17)$$

Therefore, the simplified results of the DDCS for Compton scatterings in former RIA treatments can be expressed as

$$\left(\frac{d^2\sigma}{d\omega_f d\Omega_f}\right)_{RIA} = \frac{r_0^2}{2}\frac{m}{q}\frac{\omega_f}{\omega_i}X_{KN}J(p_z) = Y_{KN}^{RIA}\cdot J(p_z). \quad (18)$$

From equations (16) and (18), it is obvious that the DDCS of Compton scattering in former RIA treatments factorizes into two parts similar to equation (3),

$$\left(\frac{d^2\sigma}{d\omega_f d\Omega_f}\right)_{RIA} = Y^{RIA}\cdot J(p_z). \quad (19)$$

The correction factor $J(p_z)$, which incorporates ground state electron momentum distribution, is called the atomic Compton profile

$$J(p_z) \equiv \int \rho(\boldsymbol{p})dp_x dp_y. \quad (20)$$

For most of the atomic systems, the momentum distribution is spherically symmetric, then the atomic Compton profile reduces to

$$J(p_z) = 2\pi\int_{|p_z|}^{\infty} p\rho(p)dp. \quad (21)$$

In these cases, the Compton profile $J(p_z)$ is bell-shaped and axisymmetric around the $p_z = 0$ axis. We restrict ourselves to the spherically symmetric case in this study.

From the procedures described above, we can notice that there are similarities among several former RIA treatments for Compton scattering. The kernel function approximations $X(K_i, K_f) \approx X_{KN}$ and $X(K_i, K_f) \approx \overline{X}(p_z)$, together with the factorization result equation (19), are the key features for former RIA treatments. Currently, these former RIA treatments are still directly used in theoretical and simulative studies [24, 25, 47]. Moreover, large numbers of interdisciplinary works in condensed matter physics and material science focusing on electron correlations [1, 2], electron momentum distributions [3–5, 21], band structures, and Fermi surfaces [6, 23], are based on these approximations. In the next subsection, we introduce an 'exact' numerical approach to calculate the DDCS of Compton scattering, which does not utilize the above-mentioned kernel function approximations and the factorization results. Therefore, in principle, our approach is more precise than those of former RIA treatments. Furthermore, the validity of the above kernel function approximations and the factorization results, which have been widely adopted in former RIA treatments as well as interdisciplinary studies, can be rigorously tested using our 'exact' numerical approach.

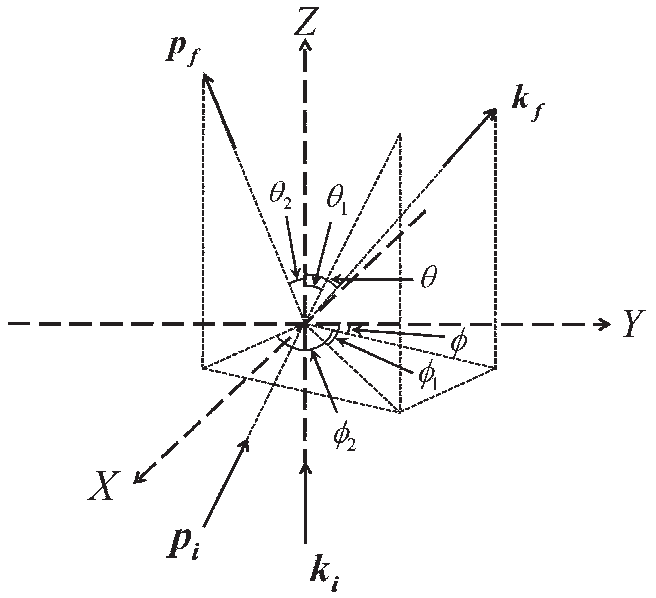

Figure 3. Coordinate system *XYZ* used in the numerical evaluation. The *Z* axis is chosen to be the direction of initial photon $\boldsymbol{k}_i$ similar to figure 2. The direction of the scattered photon is denoted as $\boldsymbol{k}_f = (k_f, \theta, \phi)$, and the vectors $\boldsymbol{p}_i = (p_i, \theta_1, \phi_1)$ and $\boldsymbol{p}_f = (p_f, \theta_2, \phi_2)$ represent the momentum of the initial state and final state electrons.

2.2. 'Exact' numerical treatments

In this section, we describe our 'exact' numerical treatment for RIA formulation. Instead of treating the kernel function $X(K_i, K_f)$ to be a slow-varying function in the integration as Ribberfors *et al* expected, we directly evaluate the integral in equation (4) through a numerical scheme.

The geometry of the Compton scattering process efficient to numerical evaluation is illustrated in figure 3. We chose a coordinate system *XYZ* such that the incoming photon moves towards the *Z* direction; the azimuthal angle and polar angle for the outgoing photon, initial electron, and final electron are denoted as (θ, ϕ), (θ_1, ϕ_1), (θ_2, ϕ_2), respectively. By employing such a coordinate system, the functions K_i and K_f can be calculated as

$$K_i = K_i(p_i, \theta_1) = \frac{E_i\omega_i}{c^2} - \frac{\omega_i p_i\cos\theta_1}{c} \quad (22)$$

$$K_f = K_f(p_i, \theta_1) = K_i(p_i, \theta_1) - \frac{\omega_i\omega_f(1-\cos\theta)}{c^2}. \quad (23)$$

From the energy and momentum conservations in the Compton scattering process, the energy of the scattered electron is given by

$$E_f = E_f(p_i, \theta_1, \phi_1) = \sqrt{p_i^2c^2 + m^2c^4 + \omega_i^2 + \omega_f^2 - 2\omega_i\omega_f\cos\theta + 2p_ic\omega_i\cos\theta_1} \times \sqrt{-2p_ic\omega_f[\cos\theta\cos\theta_1 + \sin\theta\sin\theta_1\cos(\phi - \phi_1)]}. \quad (24)$$

For simplicity, in this work, we only restrict ourselves to spherically symmetric atomic systems, and more complicated molecular or condense matter systems are not taken into consideration. In our numerical calculations, the DF theory is used to achieve the ground state wavefunctions and the electron's momentum distribution. Since spherically symmetric atomic systems are considered, the electron's momentum distribution reduces to $\rho(\boldsymbol{p}_i) = \rho(p_i)$. In the DF theory, the wavefunction of an individual electron is given by the Dirac orbital $u_{njl}(r)$, which is composed of a large component G_{njl} and a small component F_{njl}. Then the corresponding large and small components of momentum wavefunctions are given by the following Fourier transformation:

$$\phi^G_{njl}(p) = \sqrt{\frac{2}{\pi}}\int_0^\infty G_{nlj}(r)j_l(pr)r^2dr \quad (25)$$

$$\phi^F_{njl}(p) = \begin{cases} \sqrt{\frac{2}{\pi}}\int_0^\infty F_{njl}(r)j_{l+1}(pr)r^2dr & j = l + \frac{1}{2} \\ \sqrt{\frac{2}{\pi}}\int_0^\infty F_{njl}(r)j_{l-1}(pr)r^2dr & j = l - \frac{1}{2} \end{cases} \quad (26)$$

and the total momentum distribution can be calculated through

$$\rho(p_i) = \sum_a |\phi_a(p_i)|^2 = \sum_{njl} N_{njl}((\phi^G_{njl}(p_i)^2 + (\phi^F_{njl}(p_i)^2) \quad (27)$$

where N_{njl} is the number of electrons in each orbital (njl). Detailed descriptions of the Dirac orbital $u_{njl}(r)$ as well as its large and small components are given in appendix A.

Putting equations (22), (23) and (27) into the integration in equation (4), and taking the atomic binding energies into account, we obtain the DDCS for the Compton scattering processes

$$\frac{d^2\sigma}{d\omega_f d\Omega_f} = \sum_{njl}\frac{d^2\sigma_{njl}}{d\omega_f d\Omega_f} = \sum_{njl}\frac{r_0^2}{2}\frac{\omega_f}{\omega_i}m^2c^4\Theta(\omega_i - \omega_f - E^B_{njl})N_{njl} \times \int p_i^2 dp_i \sin\theta_1 d\theta_1 d\phi_1((\phi^G_{njl}(p_i)^2 + (\phi^F_{njl}(p_i)^2) \times \frac{X(K_i(p_i, \theta_1), K_f(p_i, \theta_1))}{E_i(p_i)E_f(p_i, \theta_1, \phi_1)} \times \delta(E_i + \omega_i - E_f - \omega_f) \quad (28)$$

where E^B_{njl} is the binding energy of orbital (njl), and $\Theta(\omega_i - \omega_f - E^B_{njl})$ is the Heaviside step function. When the energy transfer $T = \omega_i - \omega_f$ is less than the atomic binding energy E^B_{njl}, the Heaviside step function vanishes the cross section from this orbital (njl). In other words, the electron in this orbital is inactive in the atomic Compton scattering process $\hbar\omega_i + A \longrightarrow \hbar\omega_f + e^- + A^+$.

In order to get the results of the DDCS numerically, one point should be mentioned. In equation (28), when integrating one of the three variables p_i, θ_1 and ϕ_1, the Dirac delta function $\delta(E_i + \omega_i - E_f - \omega_f)$ in the integrand restricts this variable to a fixed value. The fixed values $\tilde{p}_i$, $\tilde{\theta}_1$ or $\tilde{\phi}_1$ can be solved by finding the zeros of function

$$f(p_i, \theta_1, \phi_1) = E_i(p_i) + \omega_i - E_f(p_i, \theta_1, \phi_1) - \omega_f \quad (29)$$

where $E_i(p_i) = \sqrt{p_i^2c^2 + m^2c^4}$ and $E_f(p_i, \theta_1, \phi_1)$ are calculated in equation (24)

To evaluate the integral in equation (28), we first integrate over the azimuthal angle ϕ_1. After some redundant calculations routinely, we get the DDCS for Compton scatterings:

$$\frac{d^2\sigma}{d\omega_f d\Omega_f} = \sum_{njl}\frac{r_0^2}{2\omega_i\sin\theta}m^2c^4\Theta(\omega_i - \omega_f - E^B_{njl})N_{njl} \times \int p_i dp_i d\theta_1((\phi^G_{njl}(p_i)^2 + (\phi^F_{njl}(p_i)^2) \times \frac{X(K_i(p_i, \theta_1), K_f(p_i, \theta_1))}{E_i(p_i) \times c\sqrt{1 - \cos^2(\phi - \tilde{\phi}_1)}} \quad (30)$$

where the fixed azimuthal angle $\tilde{\phi}_1$ satisfies

$$\cos(\phi - \tilde{\phi}_1) = \frac{\omega_i^2 + \omega_f^2 - 2\omega_i\omega_f\cos\theta}{2p_ic\omega_f\sin\theta\sin\theta_1} - \frac{(\omega_i - \omega_f)^2}{2p_ic\omega_f\sin\theta\sin\theta_1} - \frac{(\omega_i - \omega_f)E_i(p_i)}{p_ic\omega_f\sin\theta\sin\theta_1} + \frac{\cos\theta_1(\omega_i - \omega_f\cos\theta)}{\omega_f\sin\theta\sin\theta_1}. \quad (31)$$

Moreover, it is worth noting that only those which satisfy equation (31) and the inequality $-1 \leqslant \cos(\phi - \tilde{\phi}_1) \leqslant 1$ simultaneously can be regarded as physical allowed values of $\tilde{\phi}_1$.

In this work, we adopt the aforementioned order of integration in the numerical evaluation of equation (28). However, equivalent results can be achieved by exchanging the order of integration. Results obtained from alternative order of integration are given in appendix B.

3. Results and discussions

In this section, we provide the results of atomic Compton scattering obtained using our 'exact' numerical method of RIA, as described in section 2.2. For a comprehensive study, we chose four neutral atoms C, Cu, Ge, and Xe to represent the small-Z, middle-Z, and large-Z regimes. Section 3.1 is focused on differential cross sections, where a detailed comparison of our results and those of former treatments of RIA is

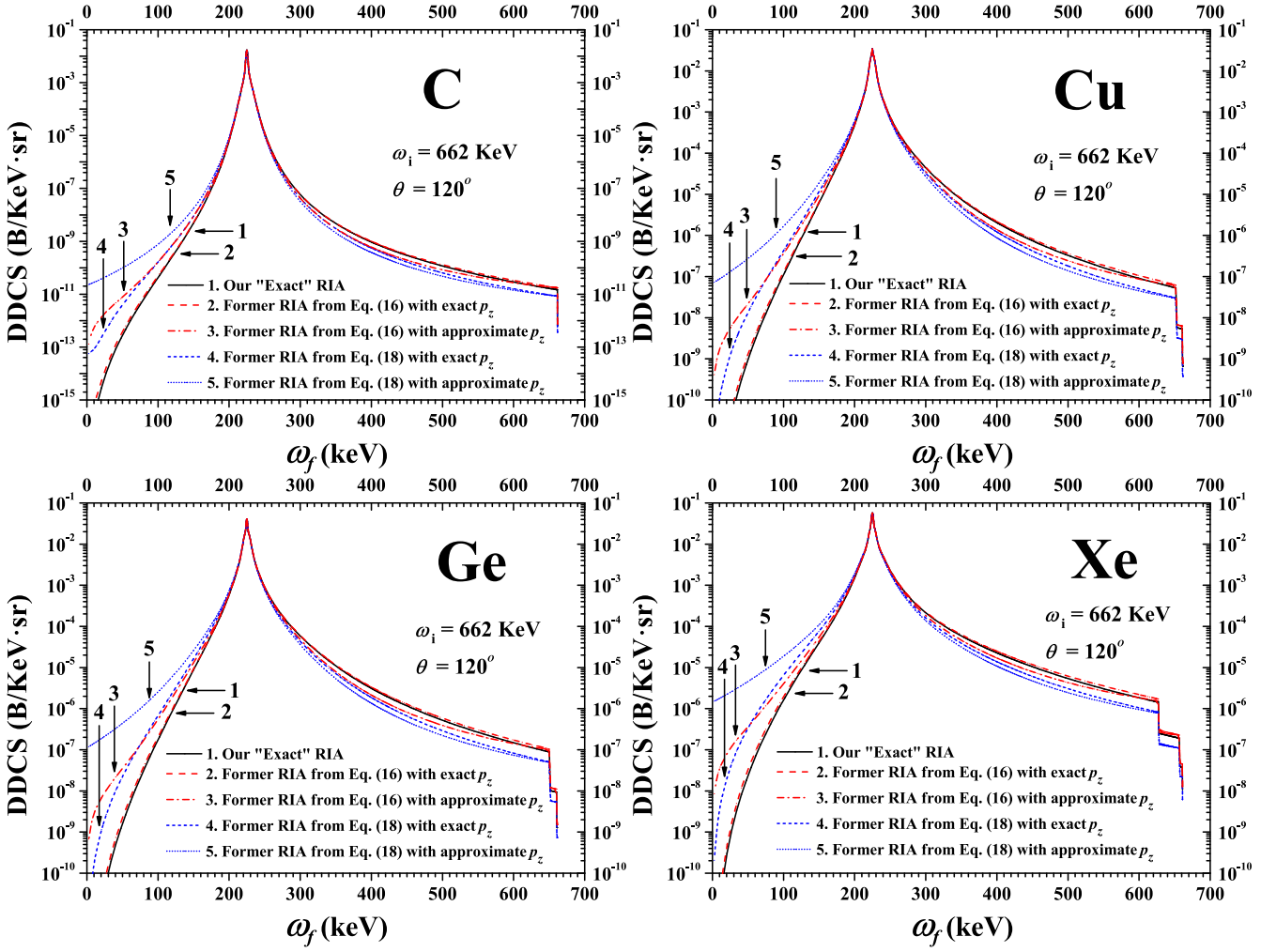

Figure 4. DDCS of Compton scattering obtained for C, Cu, Ge and Xe atoms at photon energy $\omega_i = 662$ KeV and scattering angle $\theta = 120°$. The results of our method and those of several former treatments of RIA are shown. The curves in this figure represent: 1) solid lines—the results of our 'exact' RIA treatment; 2) dashed lines—the results of former RIA treatment employing equation (16) with exact p_z values calculated in equation (10); 3) dashed-dotted lines—the results of former RIA treatment utilizing equation (16) with approximate p_z values computed in equation (12); 4) short-dashed lines—the results of former RIA treatment using equation (18) with exact p_z values; 5) short-dotted curves—the results of former RIA treatment using equation (18) with approximate p_z values.

presented. The validity of the factorization in equation (3) and the available ranges of former RIA treatments are discussed using this comparison. In section 3.2, ECPs are extracted from our results to quantitatively illustrate the differences between our method and former RIA treatments. Furthermore, we provide an uncertainty estimate for the numerical scheme in section 3.3.

3.1. Differential cross sections

In this subsection, we focus on the differential cross sections in atomic Compton scatterings. The DDCS of Compton scatterings for C, Cu, Ge, and Xe atoms at photon energies $\omega_i = 662$ KeV, 356 KeV and a scattering angle $\theta = 120°$ are shown in figures 4 and 5. Comparative results of our 'exact' numerical treatment of RIA and several former treatments of RIA have been illustrated in this figure. The results of former RIA treatments are obtained using equations (16) and (18), where the DDCS of Compton scatterings is factorized into Y times atomic Compton profiles J, similar to equation (3). Moreover, when computing the atomic Compton profiles, the momentum component p_z can be calculated using its exact or approximate values obtained from equations (10) and (12). Our 'exact' RIA results are obtained by directly evaluating the numerical integral in equation (4).

The numerical results in figures 4 and 5 show that the DDCS of Compton scattering at photon energies 662 KeV and 356 KeV are very similar, except that the locations of Compton peaks are shifted. The results in these figures indicate that our 'exact' RIA results confirm the results of former RIA treatments near the Compton peak region $\omega_f \approx \omega_C$. Thus, we can draw the conclusion that the factorization treatments adopted in former RIA studies do not change the physical results significantly in the Compton peak region, as Ribberfors *et al* expected [17, 19, 20]. Furthermore, recent works have indicated that the available range of former RIA treatments is only near the Compton peak region, where the momentum component p_z in the scattering process is not very

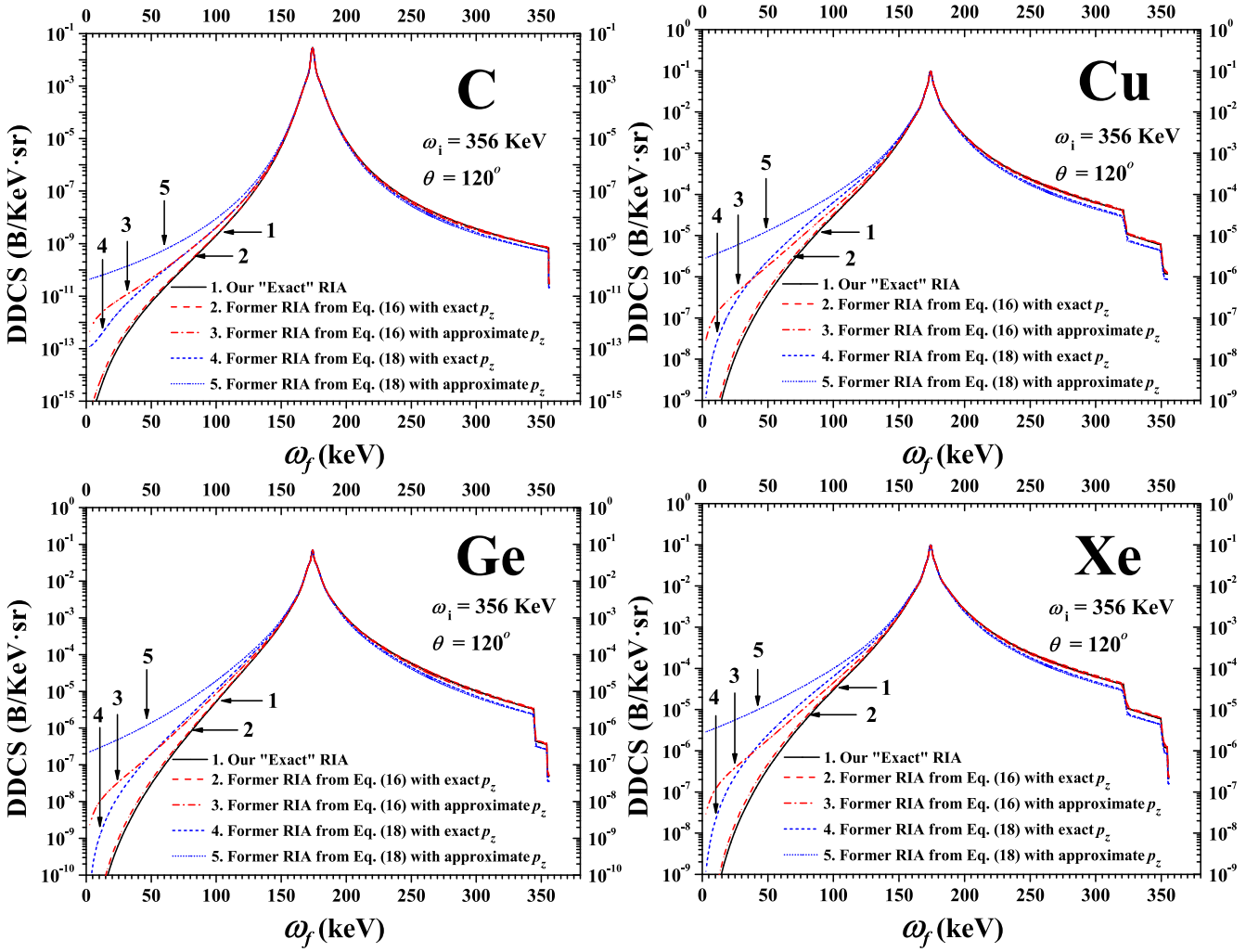

Figure 5. DDCS of Compton scattering obtained for C, Cu, Ge and Xe atoms at photon energy $\omega_i = 356$ KeV and scattering angle $\theta = 120°$. The results of our 'exact' RIA treatment and several former RIA treatments are plotted similar to those in figure 4.

large [7, 48–51]. This criterion can be demonstrated by comparison with more advanced approaches, such as the S-matrix approach. Therefore, in the region where the RIA formulation is believed to be valid, the factorization treatments, as well as kernel function approximations, used in former RIA studies still hold, and produce only a few deviations in the integration of the DDCS. Since most of interdisciplinary studies in condensed matter physics and material science using former RIA treatments consider only the cases near the Compton peak region, they are reliable at a sufficient accuracy [1–6, 21–23]. In appendix E, we have provided comparative results on the DDCS of Compton scattering between RIA and S-matrix approaches.

However, when the energy of a scattered photon is far from the Compton peak region, discrepancies between our 'exact' RIA treatment and several former RIA treatments become notable. Therefore, some factorization treatments and kernel function approximations used in former RIA studies are invalid in this region; in addition, they produce non-negligible deviations in the integration of the DDCS. Moreover, when $\omega_f < \omega_C$, former RIA treatments overestimate the DDCS of Compton scattering, whereas in the region $\omega_f > \omega_C$, our results obtain larger cross sections than the former RIA results. In several former RIA treatments, both the approximations of the kernel function $X(K_i, K_f)$ and the values of momentum component p_z significantly impact the DDCS of Compton scattering. Among the former treatments of RIA, only one approach utilized more accurate kernel function approximation $X(K_i, K_f) \approx \overline{X}(p_z)$ with the exact momentum component p_z values, which correspond to dashed curves in figures 4 and 5; this agrees well with our approach in the entire energy spectrum. Further, in appendix E, through comparisons with theoretical S-matrix calculations and experimental results, we can observe that the available range of our 'exact' RIA treatment is still only near the Compton peak, which is similar to that in former RIA treatments. In regions far from the Compton peak, our approach, despite employing an exact scheme in the numerical integration, does not exhibit a significant improvement over the former RIA treatments.

To directly validate the former RIA treatments using the kernel function, we numerically study the function $X(K_i, K_f)$ in equation (7), and the results are provided in appendix C. A detailed analysis indicates that the kernel approximation

$X(K_i, K_f) \approx X_{KN}$ in former RIA treatments works well only in the Compton peak region $\omega_f \approx \omega_C$. When the final photon energy reaches far beyond the Compton peak region, the kernel function approximation $X(K_i, K_f) \approx X_{KN}$ becomes inappropriate. The result is consistent with our conclusion obtained from the DDCS of Compton scattering in figures 4 and 5, where the results of former RIA treatments based on the approximation $X(K_i, K_f) \approx X_{KN}$ through equation (18) exhibit notable discrepancies when the final photon energy is far from the Compton peak region, irrespective of the employment of exact or approximate p_z values. For comparison, in appendix C we demonstrate that $X(K_i, K_f) \approx \overline{X}(p_z)$ is a more accurate kernel function approximation than $X(K_i, K_f) \approx X_{KN}$ when the outgoing photon energy is far from the Compton peak region. Moreover, this conclusion can be revealed from the DDCS of Compton scattering illustrated in figures 4 and 5, where the results of RIA treatments that depend on $X(K_i, K_f) \approx \overline{X}(p_z)$ through equation (16) show less discrepancy with our 'exact' RIA results than those employing $X(K_i, K_f) \approx X_{KN}$ through equation (18).

3.2. ECPs

To further quantitatively compare the results of our method and former RIA treatments, we define the ECPs as follows:

$$\overline{J}_{\rm eff}(p_z, \omega_i, \theta) \equiv \frac{1}{\overline{Y}^{RIA}} \frac{d^2\sigma}{d\omega_f d\Omega_f} = \frac{2}{r_0^2} \frac{E(p_z)}{mc^2} \frac{q}{m} \frac{\omega_i}{\omega_f} \frac{\frac{d^2\sigma}{d\omega_f d\Omega_f}}{\overline{X}(p_z)} \tag{32}$$

$$J_{\rm eff}(p_z, \omega_i, \theta) \equiv \frac{1}{Y_{KN}^{RIA}} \frac{d^2\sigma}{d\omega_f d\Omega_f} = \frac{2}{r_0^2} \frac{q}{m} \frac{\omega_f}{\omega_i} \frac{\frac{d^2\sigma}{d\omega_f d\Omega_f}}{X_{KN}} \tag{33}$$

where p_z is the projection of the electron's momentum on the momentum transfer direction, which is calculated by equation (10) or equation (12). The differential cross section $d^2\sigma/d\omega_f d\Omega_f$ is numerically obtained using our 'exact' RIA treatment. If former RIA treatments are adopted in calculating the differential cross sections, the ECPs automatically reduce to the conventional atomic Compton profile defined in equation (20). Therefore, the differences between the ECPs and the atomic Compton profiles quantify the deviations of our method from the former RIA treatments. Furthermore, the ECPs given in equations (32) and (33) contain more dynamical information of the Compton scattering process, and depend on three variables: the momentum component p_z, the initial photon energy ω_i, and the scattering angle θ. The atomic Compton profile, which is a single variable function of p_z, is totally determined by momentum distributions of atomic systems, irrespective of the dynamical properties of Compton scattering.

In this work, we use the differences between ECPs and the atomic Compton profile to quantitatively describe the differences between our 'exact' RIA results and the former RIA treatments. However, it must be noted that the above-mentioned ECPs not only act as theoretical subjects but also can be directly measured from experiments. To experimentally determine these ECPs, we must first measure the differential cross section in real Compton scattering experiments, and then substitute them in equations (32) and (33).

Before a detailed analysis of the ECPs, a briefing of the variable p_z is required. As discussed in section 2.1, the momentum component p_z can be calculated in its exact form from equation (10) or in its approximate form from equation (12). The momentum component p_z, when combined with two ECPs $\overline{J}_{\rm eff}(p_z, \omega_i, \theta)$ and $J_{\rm eff}(p_z, \omega_i, \theta)$ defined in equations (32) and (33), produce four different ECPs. These four ECPs, in comparison with the conventional atomic Compton profile defined in equation (20), can quantitatively describe the discrepancies between our 'exact' RIA calculations with the four former RIA treatments presented in figures 4 and 5, respectively.

The numerical results of ECPs at photon energy $\omega_i = 356$ KeV and scattering angle $\theta = 120°$ are very similar to those of ECPs at $\omega_i = 662$ KeV and $\theta = 120°$. Therefore, we only present the results which correspond to $\omega_i = 662$ KeV and $\theta = 120°$ in figure 6 for C, Cu, Ge, and Xe atoms. In addition, the atomic Compton profiles computed using equation (20) based on the nonrelativistic Hartree–Fock (HF) theory and the relativistic DF theory are presented for comparison. Earlier, Biggs *et al* calculated the atomic Compton profile using the nonrelativistic HF theory and the relativistic DF theory for light elements $Z < 36$ and heavy elements $Z > 36$, respectively [52]. To compare the nonrelativistic and relativistic results, we recalculate the atomic Compton profiles for C, Cu, and Ge atoms using the relativistic DF theory. We find that, for small-Z element C with weak relativistic effect, no significant difference exists between the nonrelativistic and relativistic results. However, for the middle-Z elements Cu and Ge, the relativistic effects become stronger and obvious differences exist between nonrelativistic and relativistic results for large values of $|p_z|$. Moreover, to quantitatively analyze the discrepancies between the ECPs and the atomic Compton profiles, we define the relative discrepancy as follows:

$$D \equiv \frac{J_{\rm eff} - J}{J} \tag{34}$$

where J and $J_{\rm eff}$ represent the atomic Compton profile and the ECP, respectively. To equally consider the relativistic effects, we mark only the relative discrepancies between the ECPs in RIA and the relativistic atomic Compton profiles calculated using the DF theory. However, the relative discrepancies between the ECPs and the nonrelativistic atomic Compton profiles, which are given by Biggs *et al* [52], have the same order of magnitude.

An important observation can be made from this figure, which has significant importance in interdisciplinary studies—when the momentum component $|p_z|$ is less than 10 a.u., all the ECPs converge to the atomic Compton profiles with relative discrepancies $|D| < 20\%$. A non-negligible 20% change of the variable D arises only outside the palm of the momentum component $|p_z|$ greater than 10 a.u. Therefore, previous studies on condensed matter physics and material science, which studied electron correlations, electron momentum distributions, and Fermi surfaces using Compton profiles and Compton

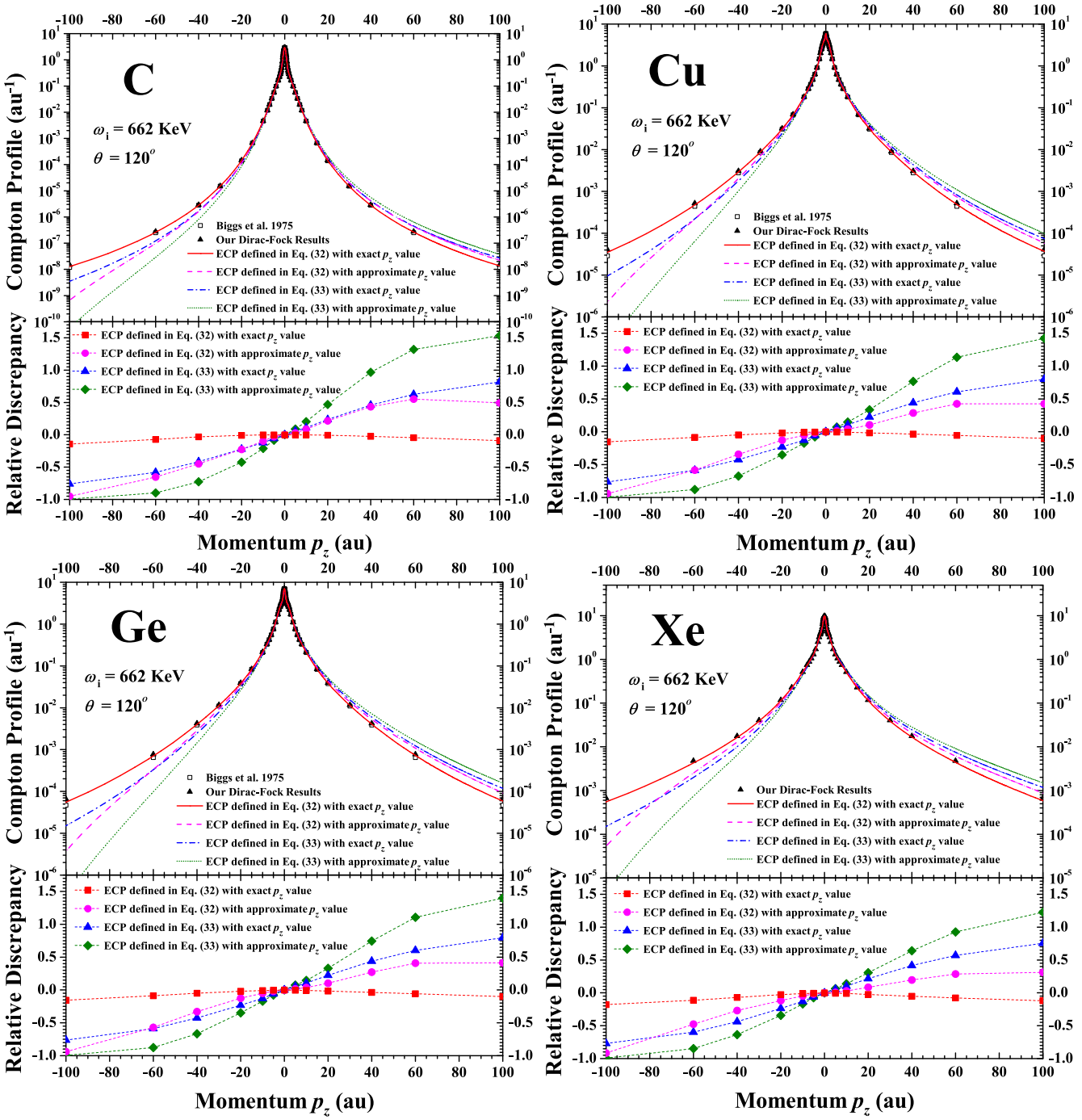

Figure 6. ECPs for C, Cu, Ge, and Xe atoms at a photon energy $\omega_i = 662$ KeV with a scattering angle $\theta = 120°$. The solid lines correspond to the ECPs $\overline{J}_{\rm eff}(p_z, \omega_i, \theta)$ defined in equation (32) with exact p_z values calculated in equation (10). The dashed lines correspond to the ECPs $\overline{J}_{\rm eff}(p_z, \omega_i, \theta)$ defined in equation (32) with approximate p_z values computed in equation (12). The dashed-dotted lines represent the ECPs $J_{\rm eff}(p_z, \omega_i, \theta)$ defined in equation (33) with exact p_z values calculated in equation (10). The short-dotted lines represent the ECPs $J_{\rm eff}(p_z, \omega_i, \theta)$ defined in equation (33) with approximate p_z values computed in equation (12). In addition, the atomic Compton profiles computed using equation (20) based on the nonrelativistic HF theory and the relativistic DF theory are presented. The HF results are provided by Biggs *et al* for $Z < 36$ [52], and the DF results are computed using our program. Moreover, the relative discrepancies, which are defined as $D \equiv (J_{\rm eff}-J)/J$ with J and $J_{\rm eff}$ as the atomic and ECPs, are superimposed in the figure for various ECPs.

scattering experiments [1–6, 21–23], are still valid with a sufficiently high accuracy, because they are mainly focused on the region $|p_z| \sim$ a.u.. However, in the large $|p_z|$ regions, except for the ECPs $\overline{J}_{\rm eff}(p_z, \omega_i, \theta)$ defined in equation (32) that employ exact p_z values, other ECPs have large discrepancies with the atomic Compton profiles in the large momentum $|p_z|$ region, especially in the negative axis of p_z. The result is consistent with the conclusions obtained from the DDCS in section 3.1, where large $|p_z|$ values corresponded to the cases where the final photon energy ω_f is far away from the Compton

Table 1. Comparative results of atomic Compton profiles for Ge and Xe atoms. Our results and those of Biggs *et al* [52] are listed in the table. The deviation parameter is defined as $D_0 \equiv |(J_0-J)/J_0|$ to characterize the uncertainties for different numerical schemes.

Ge			
p_z (a.u.)	Biggs *et al*	Our	Deviation D_0
0	7.03	7.043 9	2.0×10^{-3}
0.5	5.10	5.096 0	7.9×10^{-4}
1	3.48	3.472 1	2.3×10^{-3}
2	2.58	2.583 2	1.2×10^{-3}
5	7.59×10^{-1}	$7.589\,9 \times 10^{-1}$	8.3×10^{-6}
10	2.1×10^{-1}	$2.138\,3 \times 10^{-1}$	1.8×10^{-2}
20	3.8×10^{-2}	$3.845\,8 \times 10^{-2}$	1.2×10^{-2}
40	3.9×10^{-3}	$3.856\,3 \times 10^{-3}$	1.1×10^{-2}
Xe			
p_z (a.u.)	Biggs *et al*	Our	Deviation D_0
0	9.74	9.737 2	2.9×10^{-4}
0.5	8.21	8.212 1	2.5×10^{-4}
1	5.45	5.451 0	1.9×10^{-4}
2	3.68	3.678 2	4.9×10^{-4}
5	1.30	1.297 1	2.3×10^{-3}
10	5.1×10^{-1}	$5.150\,5 \times 10^{-1}$	9.9×10^{-3}
20	1.2×10^{-1}	$1.172\,3 \times 10^{-1}$	2.3×10^{-2}
40	1.8×10^{-2}	$1.753\,8 \times 10^{-2}$	2.6×10^{-2}

peak region. In these cases, our results of the DDCS are notably different from those of the former RIA treatments. Another interesting phenomenon revealed by figure 6 is that, unlike the atomic Compton profiles, ECPs are generally not axisymmetric around the $p_z = 0$ axis.

Furthermore, in the present work, we calculate all the ECPs at different initial photon energies ω_i and scattering angles θ, and the results are presented in appendix D. It is observable that the ECP $J_{\rm eff}(p_z, \omega_i, \theta)$ defined in equation (33) is more sensitive to the scattering angle θ than the incoming photon energy ω_i. Moreover, the ECPs $J_{\rm eff}(p_z, \omega_i, \theta)$ obtained for a smaller scattering angle θ have less discrepancy with the usual atomic Compton profiles; see appendix D for more information.

3.3. Numerical uncertainty estimate

To provide an uncertainty estimate for different numerical schemes, we recalculate the atomic Compton profiles by employing the same HF method as did Biggs *et al* in [52]. The comparative results obtained for Ge and Xe atoms are provided in table 1 for selected p_z momenta. The relative difference between our results and those in [52] provide an uncertainty estimate for different numerical schemes, and can be parameterized by the deviation parameter

$$D_0 \equiv |\frac{J_0 - J}{J_0}| \tag{35}$$

where J and J_0 correspond to the nonrelativistic atomic Compton profiles obtained from our calculations and Biggs *et al* [52], respectively. This table clearly indicates that the uncertainties for different numerical schemes are in the range 10^{-4}–10^{-2}, which is significantly less than the relative discrepancies D between the atomic Compton profiles and the ECPs obtained in section 3.2. Therefore, the uncertainties for different numerical schemes are neglected in this study.

4. Conclusions and perspectives

In this study, we develop an 'exact' numerical scheme to directly evaluate the integral to calculate the DDCS of the Compton scattering process in RIA formulation. Our method does not invoke any further simplified approximation or factorization treatment used in former RIA studies. The Compton scatterings for atomic systems are carefully analyzed in this work, and our results are effectively compared with those of former treatments of RIA. Further, the validity of further simplified approximations and factorization results used in former RIA treatments can be tested using our approach. We select four typical elements C, Cu, Ge, and Xe in this study to represent the small-Z, middle-Z, and large-Z regimes.

For the DDCS of Compton scatterings, our results agree well with those of former RIA treatments when $\omega_f \approx \omega_C$. Therefore, in the Compton peak region, where the RIA formulation is believed to be valid and reliable, the factorization treatments adopted in former RIA studies still hold, as Ribberfors *et al* expected earlier. However, when the scattered photon energy ω_f moves far away from the Compton peak region, notable discrepancies are observed. Some factorization treatments and kernel function approximations adopted in former RIA studies can produce large deviations in this region. In the entire energy spectrum, our results have little difference with the best of the former RIA treatments, which use the kernel function approximation $X(K_i, K_f) \approx \overline{X}(p_z)$ and employ the exact p_z value. Furthermore, comparisons with theoretical S-matrix calculations and experimental results indicate that the available ranges of the RIA formulations are near the Compton peak. In regions far from the Compton peak, the RIA results become inaccurate, even when our 'exact' numerical scheme is used.

To further quantitatively compare the differences between our 'exact' RIA results and those of former RIA treatments, various ECPs are defined and calculated in this study. Detailed results indicate that, except for the ECP $\overline{J}_{\rm eff}(p_z, \omega_i, \theta)$ defined in equation (32) by employing the exact p_z values obtained from equation (10), other ECPs exhibit notable discrepancies from atomic Compton profiles for large values of the momentum component $|p_z|$, especially in the negative axis of p_z. Furthermore, the following conclusions can be drawn from the analysis of ECPs for various incident photon energies ω_i and scattering angles θ:

(i). The ECPs do not show any notable difference from the atomic Compton profiles for a small momentum value $|p_z| < 10$ a.u.. A non-negligible 20% change of relative discrepancy D arises only in the large momentum cases with $|p_z| > 10$ a.u.. Therefore, the studies on condensed matter

physics and material science that are focused on electron correlation, electron momentum distribution, and Fermi surfaces using Compton profiles and Compton scattering experiments, which correspond to $|p_z| \sim$ a.u., are still valid with sufficiently high accuracy.

(*ii*). Unlike the atomic Compton profiles, the ECPs are generally not axisymmetric around the $p_z = 0$ axis.

(*iii*). The ECP $J_{\rm eff}(p_z, \omega_i, \theta)$ defined in equation (33) is more sensitive to the scattering angle θ than the incoming photon energy ω_i. Moreover, the ECP $J_{\rm eff}(p_z, \omega_i, \theta)$ obtained from a smaller scattering angle θ has less discrepancy with the usual atomic Compton profiles.

To summarize, in the present work, we conduct a comprehensive study of atomic Compton scatterings using our 'exact' numerical treatment in the RIA formulation. Despite successfully employing the 'exact' numerical evaluation for the integral in equation (4) and not introducing any kernel function approximation and factorization treatment, our approach still relies on the physical picture of RIA, which is imperfect and has limitations. For example, the DDCS of Compton scattering in the RIA approach starts from equation (4), which is, in addition, an approximation, and neglects a few interference terms in the dynamical process of Compton scattering. Some studies have indicated that the RIA approach can be realized by making leading order approximations for more advanced methods [15, 49, 50]. In the past few years, several approaches beyond the IA formulation have been investigated [7, 49–51, 53–59]. These works, which mainly employed low-energy theorems and S-matrix formulation, revealed many remarkable and nontrivial aspects of Compton scatterings and have gained significant interest in interdisciplinary studies. Accordingly, we intend to study atomic Compton scatterings beyond the IA formulation in the future.

Acknowledgments

We acknowledge helpful discussions with Shu-Kui Liu, Hao-Yang Xing, Qiang Du and Henry T Wong. This work is supported by the National Key Research and Development Program of China (No. 2017YFA0402203), the National Natural Science Foundation of China (Grants No. 11475117, No. 11474209, No. 11975159) and the Fundamental Research Funds for the Central Universities.

Appendix A. Dirac orbitals

In this appendix, we give a detailed description of the Dirac orbitals we used in section 2. In this work, we only consider spherically symmetric atomic systems. Therefore, the wavefunction of the electron state with a definite quantum number $(n\kappa m)$, which is also called the Dirac orbital, has the following form [30, 31, 60]

$$\psi_{n\kappa m}(\boldsymbol{r}) = \psi_{n\kappa m}(r, \theta, \phi) = \frac{1}{r}\begin{bmatrix} G_{n\kappa}(r)\Omega_{\kappa m}(\theta, \phi) \\ iF_{n\kappa}(r)\Omega_{-\kappa m}(\theta, \phi) \end{bmatrix} \quad \text{(A.1)}$$

where $G_{n\kappa}(r)$ and $F_{n\kappa}(r)$ are the large and small components respectively, $\Omega_{\kappa m}(\theta, \phi)$ is the normalized spherical spinor defined as:

$$\Omega_{\kappa m}(\theta, \phi) = \sum_{\mu} \langle lm - \mu; \frac{1}{2}\mu | jm\rangle Y_{lm}(\theta, \phi)\chi_{\mu} \quad \text{(A.2)}$$

where $Y_{lm}(\theta, \phi)$ is the spherical harmonics, $\langle lm - \mu; \frac{1}{2}\mu | jm\rangle$ is the Clebsch–Gordan coefficient, and χ_{μ} is a spinor with $s = 1/2$ and $s_z = \mu$.

In the above expressions, the quantum number κ is the eigenvalue of operator

$$K = \frac{1}{\hbar}\begin{pmatrix} \boldsymbol{L}\cdot\boldsymbol{\alpha} + \hbar & 0 \\ 0 & -\boldsymbol{L}\cdot\boldsymbol{\alpha} - \hbar \end{pmatrix} \quad \text{(A.3)}$$

with $\boldsymbol{L}$ denoting the orbital angular momentum vector and $\boldsymbol{\alpha}$ the conventional Dirac-α matrices. The information of orbital angular momentum l and total momentum j can be incorporated into quantum number κ [14]

$$j = |\kappa| - \frac{1}{2} \quad \text{(A.4)}$$

$$l = \begin{cases} \kappa & \kappa > 0 \\ -\kappa - 1 & \kappa < 0 \end{cases} \quad \text{(A.5)}$$

In many cases, only the radial part needs to be focused, and the angular part can be separated and neglected for simplicity. Therefore, we can introduce the following two-component radial Dirac orbitals:

$$u_{n\kappa}(r) \equiv u_{njl}(r) = \begin{bmatrix} G_{njl}(r) \\ F_{njl}(r) \end{bmatrix}. \quad \text{(A.6)}$$

After introduction of the above Dirac orbitals, as well as its large and small components $F_{n\kappa} = F_{njl}$, $G_{n\kappa} = G_{njl}$, the DF equation for core and valence electrons can be expressed and solved routinely. Therefore, we can get the ground state wavefunctions for the whole atomic systems, as well as the wavefunctions for individual electrons.

Appendix B. Equivalent results for numerical integration

In section 2.2, we mentioned that equivalent results for the DDCS can be achieved by exchanging the order of integration in equation (28). In this appendix, we present results on differential cross sections calculated using alternative orders of integration.

When we first integrate over momentum p_i or polar angle θ_1 in equation (28), the DDCS for Compton scattering

becomes

$$\frac{d^2\sigma}{d\omega_f d\Omega_f} = \sum_{njl} \frac{r_0^2}{2}\frac{\omega_f}{\omega_i} m^2c^4\Theta(\omega_i - \omega_f - E^B_{njl})N_{njl} \times \int \tilde{p}_i^2 \sin\theta_1 d\theta_1 d\phi_1((\phi^G_{njl}(\tilde{p}_i)^2 + (\phi^F_{njl}(\tilde{p}_i)^2) \times \frac{X(K_i(\tilde{p}_i,\,\theta_1),\,K_f(\tilde{p}_i,\,\theta_1,\,\phi_1))}{E_i(\tilde{p}_i)E_f(\tilde{p}_i)} \times \left|\frac{\tilde{p}_i c^2}{E_i(\tilde{p}_i)} - \frac{\tilde{p}_i c^2 + (A\sin\theta_1 - B\cos\theta_1)c}{E_f(\tilde{p}_i)}\right|^{-1} \tag{B.1}$$

$$\frac{d^2\sigma}{d\omega_f d\Omega_f} = \sum_{njl} \frac{r_0^2}{2}\frac{\omega_f}{\omega_i} m^2c^4\Theta(\omega_i - \omega_f - E^B_{njl})N_{njl} \times \int p_i dp_i d\phi_1((\phi^G_{njl}(p_i)^2 + (\phi^F_{njl}(p_i)^2) \times \left|\frac{X(K_i(p_i,\,\tilde{\theta}_1),\,K_f(p_i,\,\tilde{\theta}_1,\,\phi_1)) \times \sin\tilde{\theta}_1}{E_i(p_i) \times (A\sin\tilde{\theta}_1 + B\cos\tilde{\theta}_1)c}\right| \tag{B.2}$$

where

$$A \equiv \omega_i - \omega_f\cos\theta \tag{B.3}$$

$$B \equiv \omega_f \sin\theta\cos(\phi - \phi_1). \tag{B.4}$$

The fixed momentum $\tilde{p}_i$ and polar angle $\tilde{\theta}_1$ are calculated by solving the zeros of function f in equation (29) respectively. After tedious calculations, $\tilde{p}_i$ can be expressed as:

$$\tilde{p}_i = \frac{-MN \pm \sqrt{N^2 + (M^2 - 1)m^2c^4}}{c(M^2 - 1)} \tag{B.5}$$

where

$$M \equiv \frac{A\cos\theta_1 - B\sin\theta_1}{\omega_i - \omega_f} \tag{B.6}$$

$$N \equiv \frac{\omega_i\omega_f(1 - \cos\theta)}{\omega_i - \omega_f} \tag{B.7}$$

.Similar to the case of $\tilde{\phi}_1$ as discussed in section 2.2, only those which satisfy equation (B.5) and the inequality $\tilde{p}_i \geqslant 0$ simultaneously can be regarded as physical allowed values of $\tilde{p}_i$.

The fixed polar angle $\tilde{\theta}_1$ can be expressed through $\sin\tilde{\theta}_1$ or $\cos\tilde{\theta}_1$. The expressions for $\sin\tilde{\theta}_1$ and $\cos\tilde{\theta}_1$ are:

$$\sin\tilde{\theta}_1 = \frac{-BC \pm \sqrt{A^2(A^2 + B^2 - C^2)}}{A^2 + B^2} \tag{B.8}$$

$$\cos\tilde{\theta}_1 = \frac{B}{A}\sin\tilde{\theta}_1 + \frac{C}{A} \tag{B.9}$$

where C is defined as

$$C \equiv \frac{E_i(p_i)(\omega_i - \omega_f) - \omega_i\omega_f(1 - \cos\theta)}{p_i c} \tag{B.10}$$

.Similarly, only those which satisfy the above expressions (B.8)–(B.9) and the inequality $-1 \leqslant \sin\tilde{\theta}_1 \leqslant 1$ simultaneously are physically reasonable values of $\tilde{\theta}_1$.

Appendix C. Validity of the approximation $X(K_i, K_f) \approx X_{KN}$ and $X(K_i, K_f) \approx \overline{X}(p_z)$

In this appendix, we numerically study the kernel function $X(K_i, K_f)$ in the integrand of equation (4). Particularly, we test the validity of the approximations

$$X(K_i,\,K_f) \approx X_{KN} = \frac{\omega_i}{\omega_f} + \frac{\omega_f}{\omega_i} - \sin^2\theta \tag{C.1}$$

and

$$X(K_i,\,K_f) \approx \overline{X}(p_z) = \frac{K_i(p_z)}{K_f(p_z)} + \frac{K_f(p_z)}{K_i(p_z)} + 2m^2c^2 \times \left(\frac{1}{K_i(p_z)} - \frac{1}{K_f(p_z)}\right) + m^4c^4\left(\frac{1}{K_i(p_z)} - \frac{1}{K_f(p_z)}\right)^2 \tag{C.2}$$

used in former treatments of RIA as discussed in section 2. In order to quantitatively describe the differences between the kernel function $X(K_i, K_f)$ and its Klein–Nishina value X_{KN}, or the differences between $X(K_i, K_f)$ and its 'averaged' value $\overline{X}(p_z)$, we can define the relative factors α and β to be

$$\alpha \equiv \frac{X(K_i,\,K_f)}{X_{KN}} \tag{C.3}$$

$$\beta \equiv \frac{X(K_i,\,K_f)}{\overline{X}(p_z)}. \tag{C.4}$$

Here, the function $X(K_i, K_f)$ is calculated in equation (7); in general it depends on the initial and final photon energy ω_i and ω_f, scattering angle θ , as well as the electron pre-collision momentum $\boldsymbol{p}_i = (p_i,\,\theta_1,\,\phi_1)$. Meanwhile the 'averaged' value $\overline{X}(p_z)$ depends on momentum component p_z obtained in equation (10) or equation (12), irrespective of the transverse momentum in the xy plane. The Klein–Nishina value X_{KN} corresponds to the special case where the electrons are at rest in the target, namely $\boldsymbol{p}_i = 0$.

Before a detailed analysis, we give the electron momentum distributions $\rho(p_i)/Z$ for C, Cu, Ge and Xe atoms in figure C1. In this figure, the momentum distribution of each element is normalized to give the contribution from one electron. The momentum distributions of Cu and Ge atoms are very similar to each other and can hardly be distinguished in the logarithmic coordinate. For all the elements C, Cu, Ge and Xe, momentum distributions decrease rapidly in the large momentum region. Therefore, the large momentum region gives negligible contributions on momentum distributions, compared with the small momentum region. Since the integrand in equation (4) is proportional to the momentum distribution $\rho(p_i)$, we can draw the conclusion that the small momentum region plays a dominant role in calculating the DDCS of Compton scatterings from equation (4), while the large momentum region has tiny contributions in the integration. Contributions from the large momentum region become

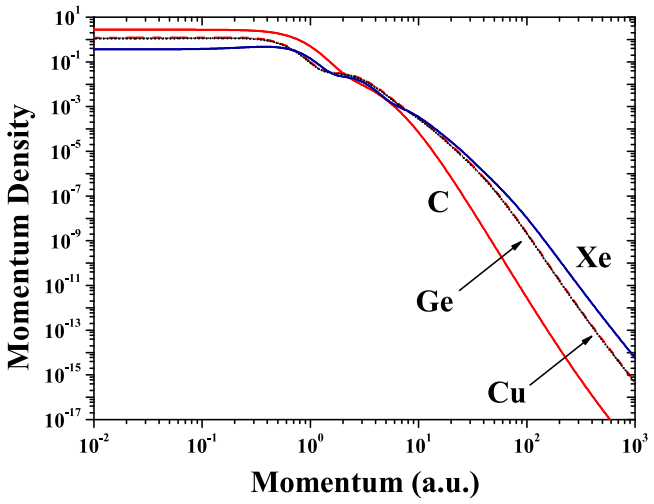

Figure C1. Electron momentum distributions $\rho(p_i)/Z$ for C, Ge, Cu and Xe atoms in the atomic units. It is worth noting that we have normalized the momentum distribution into the contribution from one electron.

notable only when the small momentum region is forbidden in the energy and momentum conservations.

We select the case $\omega_i = 662$ KeV and $\theta = 120°$ as a representative example, and present the numerical results of α and β where the final photon energy ω_f goes in and away from the Compton peak region, respectively. First, we consider the case corresponding to the Compton peak region, where the final photon energy is $\omega_f = \omega_C = 224.9$ KeV. In this condition, the momentum component is $p_z = 0$, which leads to $\overline{X}(p_z) = X_{KN}$. Therefore, the relative factors α and β coincide with each other, and only one of them needs to be analyzed quantitatively. The numerical values of factor α in this condition are shown in figure C2. The minimal value of momentum that is kinematically allowed becomes $p_i^{\min} = |p_z| = 0$ a.u.. In this figure we only plot the contributions from small momentum values $_{pi} = 0$–25 a.u., where the momentum density is sufficiently large and can give notable contributions in the integration of equation (4). This figure clearly shows that the relative factor α varies from 0.90–1.15, which indicates the kernel function approximation $X(K_i, K_f) \approx X_{KN}$ and $X(K_i, K_f) \approx \overline{X}(p_z)$ are valid and reliable in the Compton peak region. The result is consistent with conclusions obtained from figures 4 and 5, which indicated that the results of our 'exact' RIA treatment have small discrepancies with those of former RIA treatment in the Compton peak region $\omega_f \approx \omega_C$.

On the other hand, we select the conditions $\omega_f = 500$ KeV and $\theta = 120°$ to illustrate the case where the final photon energy is far away from the Compton peak region. The results of relative factors α and β are given in figures C3 and C4. A crucial difference from the previous case is that small momentum values $_{pi} < 100$ a.u. are not kinematically allowed in energy and momentum conservations. Therefore, we only plot the region where the electron momentum density has sufficiently large values. The minimal value of momentum that is kinematically allowed is $p_i^{\min} = |p_z| \approx 105$ a.u.. From these figures, we can observe that the relative factor α

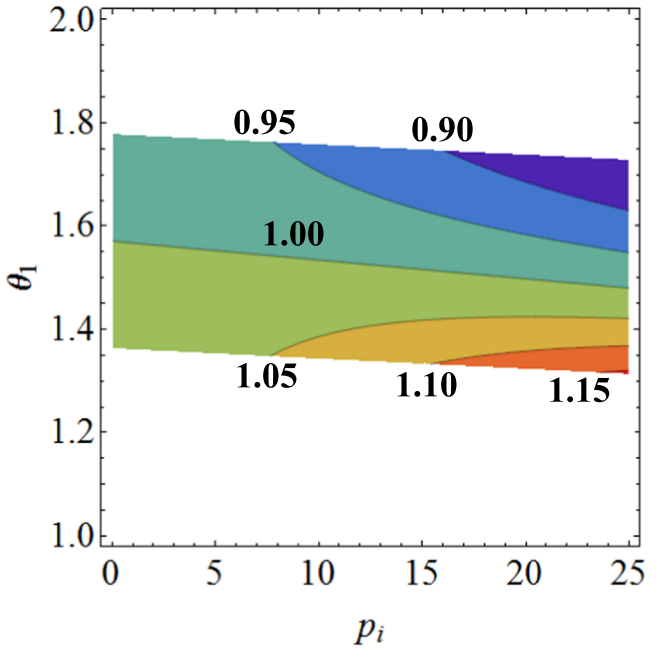

Figure C2. Counterplot of relative factor α when outgoing photon energy ω_f goes in the Compton peak region. We select the following conditions: incoming photon energy $\omega_i = 662$ KeV, outgoing photon energy $\omega_f = \omega_C = 224.9$ KeV, and scattering angle $\theta = 120°$. The horizontal axis labels the electron momentum $_{pi}$ in units of a.u., and the vertical axis labels the polar angle of electron θ_1 in units of radian. The regions which are not kinematically allowed in the energy and momentum conservations are left with white.

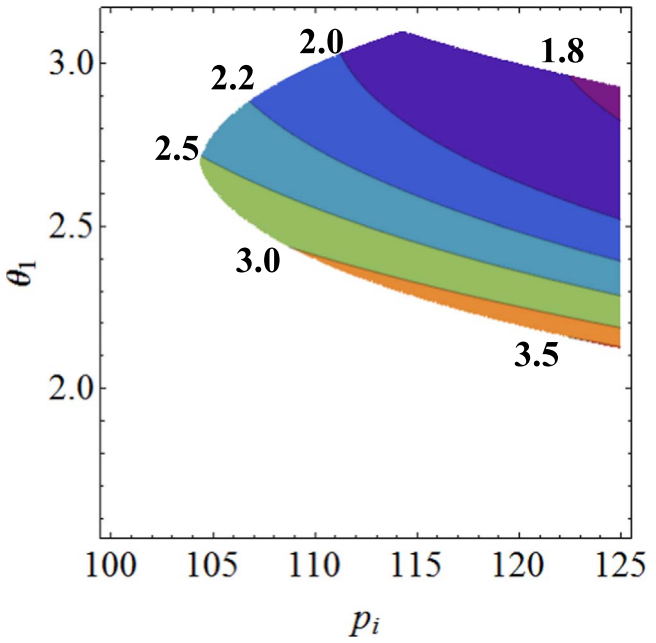

Figure C3. Counterplot of relative factor α when the final photon energy ω_f is far from the Compton peak region. We select the following conditions: initial photon energy $\omega_i = 662$ KeV, final photon energy $\omega_f = 500$ KeV, and scattering angle $\theta = 120°$. The horizontal and vertical axes label the electron momentum $_{pi}$ and polar angle θ_1 similar to that in figure C2. The regions which are not kinematically allowed in the energy and momentum conservations are left with white similar to that in figure C2.

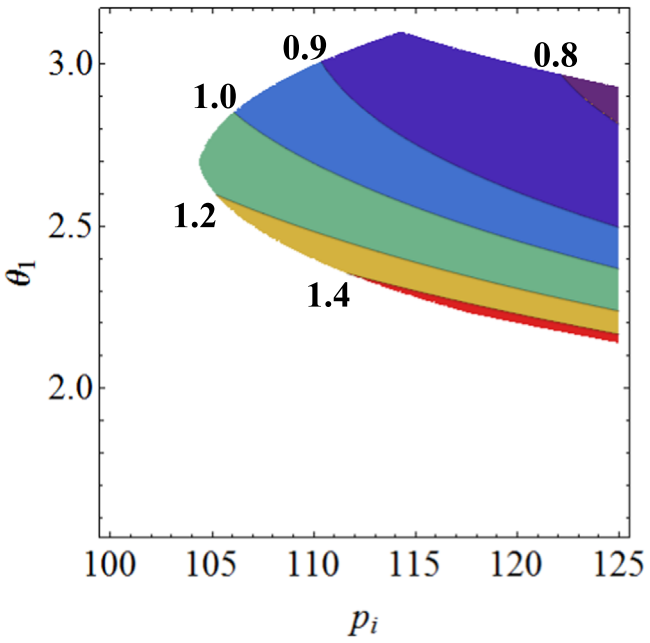

Figure C4. Counterplot of relative factor β when the final photon energy ω_f is far from the Compton peak region. We select the following conditions: initial photon energy $\omega_i = 662$ KeV, final photon energy $\omega_f = 500$ KeV, and scattering angle $\theta = 120°$. The horizontal and vertical axes label the electron momentum $_{pi}$ and polar angle θ_1 similar to that in figure C2. The regions which are not kinematically allowed in the energy and momentum conservations are left with white similar to that in figure C2.

varies from 1.8–3.5, while β is between 0.8–1.4, indicating that $X(K_i, K_f) \approx \overline{X}(p_z)$ is a better kernel function approximation than $X(K_i, K_f) \approx X_{KN}$. This result is consistent with our DDCS results obtained from figures 4 and 5 in section 3.1. The large momentum component $|p_z| \approx 105$ a.u. corresponds to the cases where the final photon energy is far away from the Compton peak region. In these conditions, the results of former RIA treatments agree with our 'exact' RIA calculations only when $X(K_i, K_f) \approx \overline{X}(p_z)$ is used to calculate the DDCS of Compton scattering with exact p_z values utilized. However, when $X(K_i, K_f) \approx X_{KN}$ is adopted to calculate the DDCS, there are large discrepancies between our results and those of former RIA treatments, irrespective of whether exact or approximate p_z values are employed.

Appendix D. More results of ECPs

In this appendix, we present more detailed numerical results of the ECPs $\overline{J}_{\rm eff}(p_z, \omega_i, \theta)$ and $J_{\rm eff}(p_z, \omega_i, \theta)$ defined in section 3.2. These results reveal some intrinsic properties of ECPs. For simplicity, we list only the results of the Ge atom. The results of C, Cu, and Xe atoms are similar to those of Ge.

The ECPs of the Ge atom at a scattering angle $\theta = 120°$ with various incident photon energies are shown in figure D1. In this work, we select several characteristic energies for gamma-ray sources: 320 KeV, 356 KeV, 511 KeV, and 662 KeV. The ECPs $\overline{J}_{\rm eff}(p_z, \omega_i, \theta)$ defined in equation (32) with approximate or exact p_z values computed in equations (12) and (10) are shown on the top. The ECPs $J_{\rm eff}(p_z, \omega_i, \theta)$ defined in equation (33) with approximate or exact p_z values are shown at the bottom. In addition, the atomic Compton profiles computed using equation (20) based on the nonrelativistic HF theory and the relativistic DF theory are presented for comparison. The relative discrepancies defined as $D \equiv (J_{\rm eff} - J)/J$ in section 3.2 are superimposed similar to that in figure 6. From this figure, we can observe that, only the ECP $\overline{J}_{\rm eff}(p_z, \omega_i, \theta)$ defined in equation (32) which employs exact p_z values fits well with the atomic Compton profiles for all values of p_z. Other ECPs are not axisymmetric around the $p_z = 0$ axis and have large discrepancies at large $|p_z|$ values, specifically in the negative axis of p_z. It is worth noting that, for various ECPs, the momentum component p_z has maximum and minimum values because of energy and momentum conservations in Compton scatterings. Moreover, for the same scattering angle θ, when the incident photon energy ω_i is low, the maximal kinematically allowed value of p_z becomes small. In all conditions, the minimum values of p_z are less than -100 a.u., which are not shown in this figure. Similar to that in section 3.2, when $|p_z| < 10$ a.u., all the ECPs are consistent with the atomic Compton profiles within 20% uncertainty of the variable D. The deviations become pronounced only when $|p_z| > 10$ a.u., which corresponds to the cases where the final photon energy ω_f is far from the Compton peak region in the DDCS spectrum. Another interesting phenomenon is that all the ECPs at different energies ω_i almost converge with each other at a fixed scattering angle $\theta = 120°$.

The ECPs of the Ge atom at photon energy $\omega_i = 662$ KeV at various scattering angles θ are shown in figure D2. We select the scattering angles $\theta = 10°$, $30°$, $60°$, $90°$, $120°$ and $150°$ in this figure. The ECPs $\overline{J}_{\rm eff}(p_z, \omega_i, \theta)$ and $J_{\rm eff}(p_z, \omega_i, \theta)$ defined in equations (32) and (33) with approximate or exact p_z values computed in equations (12) and (10) are plotted similar to figure D1. Further, the nonrelativistic and the relativistic atomic Compton profiles are included in the figure. In addition, the relative discrepancies $D \equiv (J_{\rm eff} - J)/J$ are superimposed similar to that in figures 6 and D1. In these cases, the momentum p_z has maximum and minimum values constrained by energy and momentum conservations, and the maximal kinematically allowed value of p_z increases with the increase in scattering angle θ. In these cases, only the ECP $\overline{J}_{\rm eff}(p_z, \omega_i, \theta)$ defined in equation (32) calculated using exact p_z values fits well with the atomic Compton profiles for all p_z values. Other ECPs are not axisymmetric around the $p_z = 0$ axis and show large discrepancies for large $|p_z|$ values. Figure D2 clearly indicates that the ECPs $J_{\rm eff}(p_z, \omega_i, \theta)$ defined in equation (33) for different scattering angles θ do not converge with each other at a fixed incident photon energy $\omega_i = 662$ KeV. However, figure D1 illustrates that the ECPs $J_{\rm eff}(p_z, \omega_i, \theta)$ for different photon energies ω_i converge with each other at a fixed scattering angle $\theta = 120°$. Therefore, we can draw the conclusion that the ECP $J_{\rm eff}(p_z, \omega_i, \theta)$ is more sensitive to scattering angle

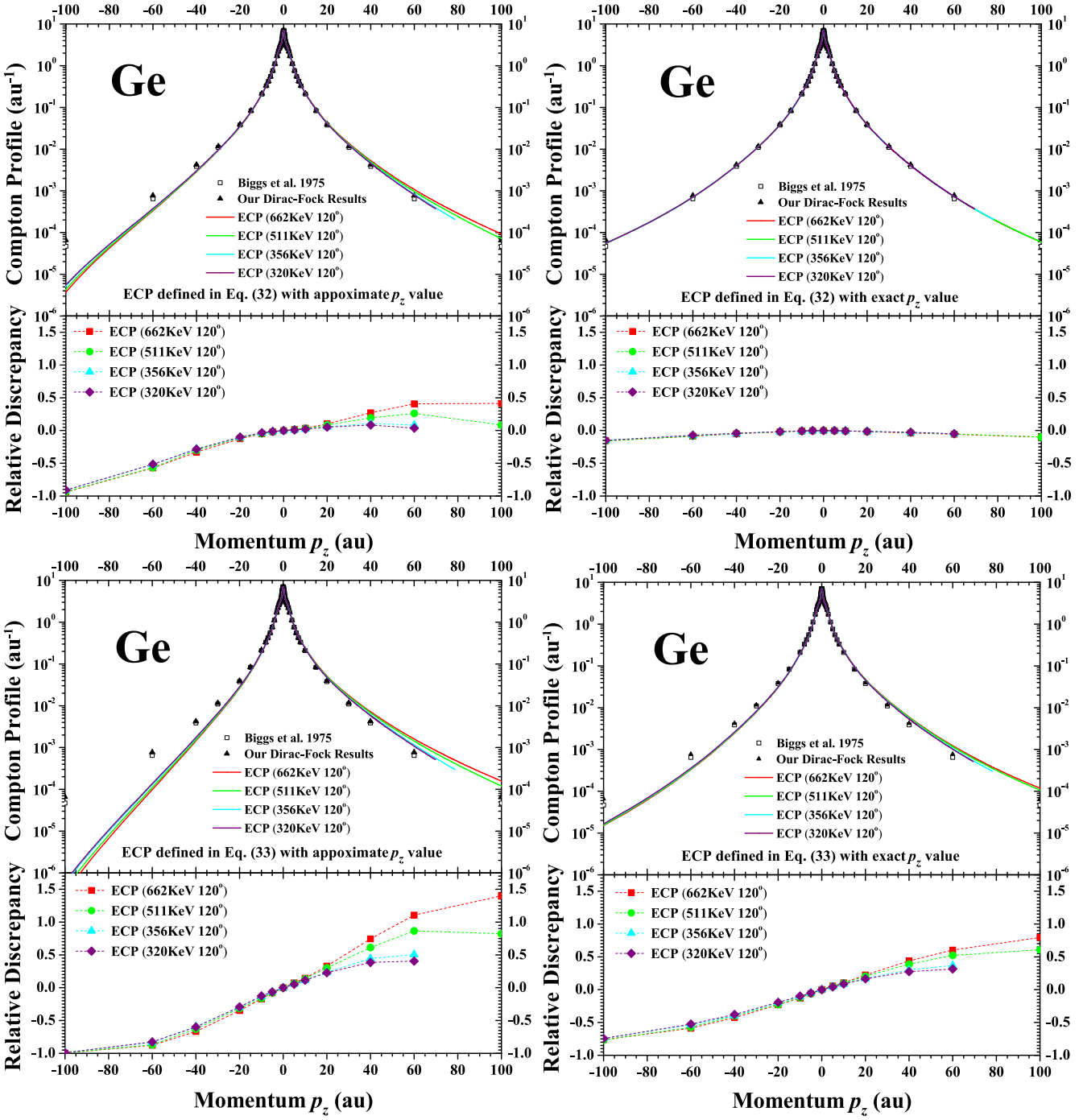

Figure D1. ECP of the Ge atom at a scattering angle $\theta = 120^\circ$ with various incident photon energies $\omega_i = 662$ KeV, 511 KeV, 356 KeV, and 320 KeV. Top left: ECP $\overline{J}_{\rm eff}(p_z, \omega_i, \theta)$ defined in equation (32) with approximate p_z values computed in equation (12). Top right: ECP $\overline{J}_{\rm eff}(p_z, \omega_i, \theta)$ defined in equation (32) with exact p_z values calculated in equation (10). Bottom left: ECP $J_{\rm eff}(p_z, \omega_i, \theta)$ defined in equation (33) employing approximate p_z values. Bottom right: ECP $J_{\rm eff}(p_z, \omega_i, \theta)$ defined in equation (33) employing exact p_z values. Atomic Compton profiles $J(p_z)$ computed using equation (20) based on the nonrelativistic HF theory and the relativistic DF theory are plotted similar to figure 6. Moreover, the relative discrepancies defined as $D \equiv (J_{\rm eff} - J)/J$ are superimposed similar to that in figure 6. It must be noted that for various ECPs, the momentum component p_z has a maximal cut-off because of energy and momentum conservations.

θ than incident photon energy ω_i. Moreover, the ECP $J_{\rm eff}(p_z, \omega_i, \theta)$ obtained from a smaller scattering angle has less discrepancy with the usual atomic Compton profiles. Furthermore, when $|p_z|$ is less than 10 a.u., all the ECPs are consistent with the atomic Compton profiles within 20% uncertainty of the variable D, similar to that in figures 6 and D1. Therefore, previous studies on condensed matter physics relating to electron correlations, electron momentum distributions, and Fermi surfaces with Compton profiles are still valid with sufficiently high accuracy [1–6, 21–23].

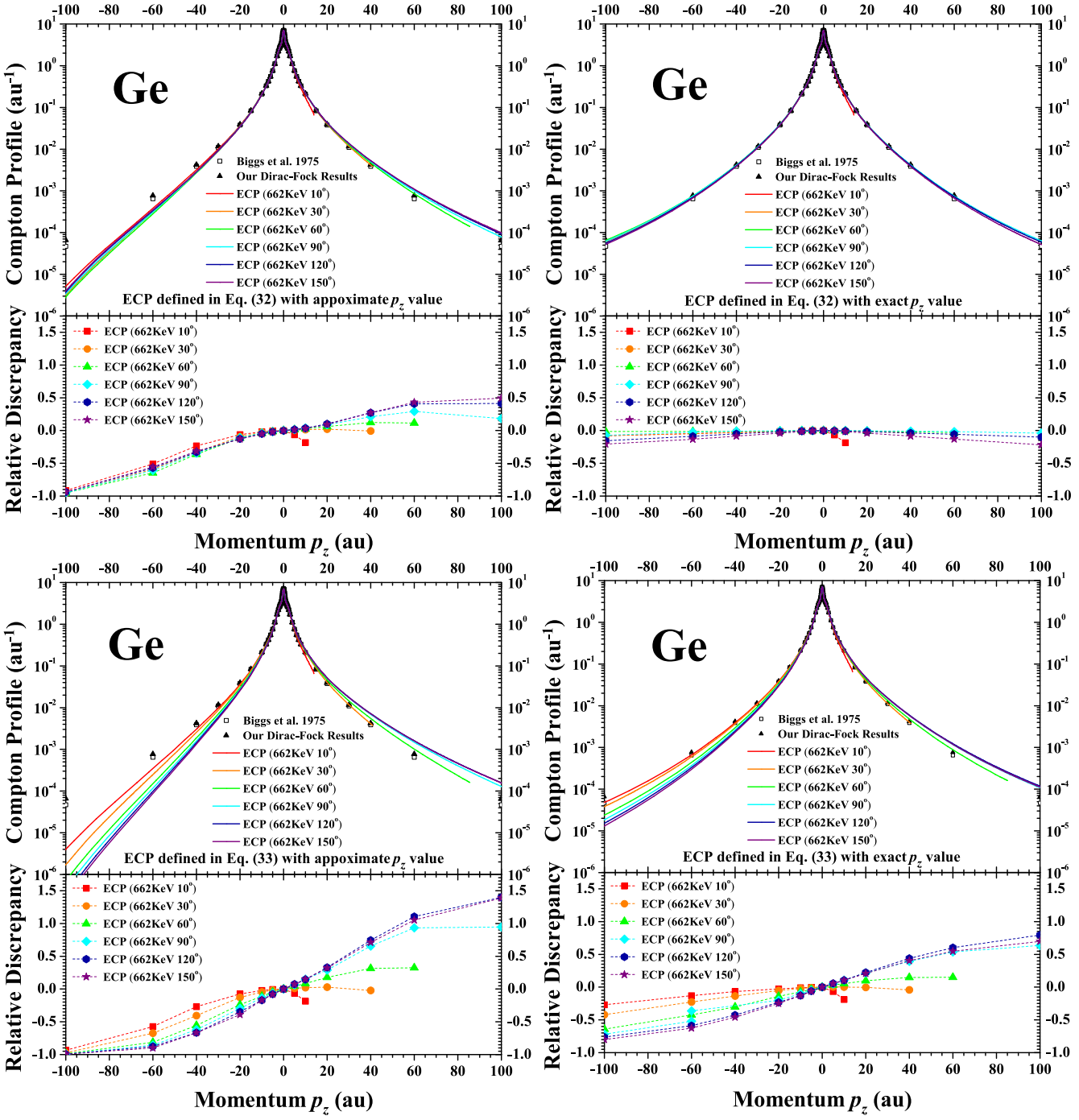

Figure D2. ECPs of the Ge atom at a photon energy $\omega_i = 662$ KeV with various scattering angles $\theta = 10°, 30°, 60°, 90°, 120°$ and $150°$. The ECPs $\overline{J}_{\rm eff}(p_z, \omega_i, \theta)$ and $J_{\rm eff}(p_z, \omega_i, \theta)$ defined in equations (32) and (33) with approximate or exact p_z values computed in equations (12) and (10) are plotted similar to that in figure D1. In addition, the atomic Compton profiles $J(p_z)$ computed using equation (20) based on nonrelativistic and relativistic theories are plotted in the figure. The relative discrepancies defined as $D \equiv (J_{\rm eff} - J)/J$ are superimposed similar to that in figures 6 and D1. It must be noted that for various ECPs, the momentum component p_z has a maximal cut-off because of energy and momentum conservations.

Appendix E. Comparison with S-matrix calculations

In this appendix, we present the comparative results of the DDCS of Compton scattering obtained from the RIA formulation and the more advanced S-matrix approach. These comparisons illustrate the available range for RIA formulation to address the atomic Compton scattering.

Figure E1 presents the comparative results for a Pb atom at an incident photon energy $\omega_i = 279$ KeV and a scattering angle $\theta = 135°$. The DDCS results for the Compton scattering process obtained using our 'exact' RIA approach and several former RIA treatments are plotted similar to figures 4 and 5. In addition, the S-matrix and the experimental results are included in this figure. The S-matrix calculations are

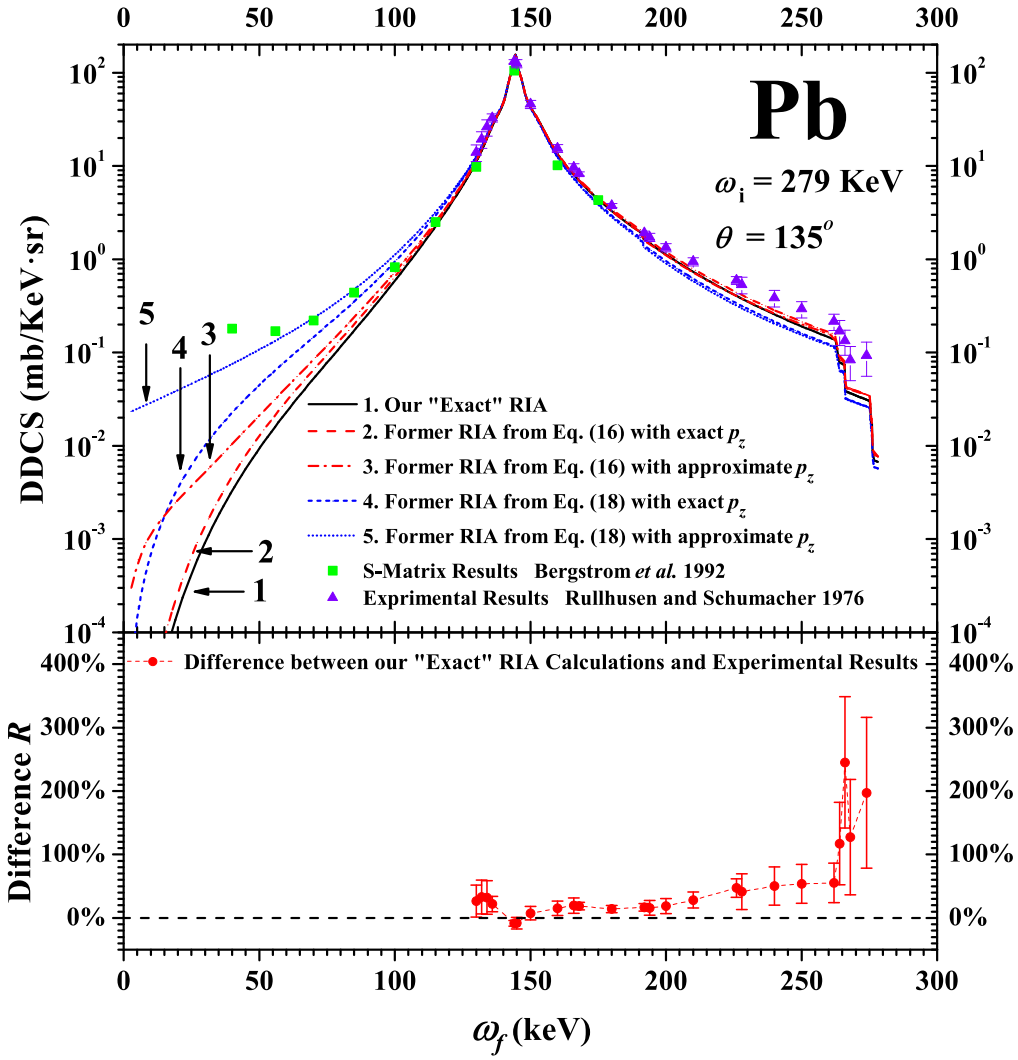

Figure E1. Comparative results of the DDCS of Compton scattering for a Pb atom obtained from RIA and S-matrix approaches. We select the following conditions: incident photon energy $\omega_i = 279$ KeV and scattering angle $\theta = 135°$. Further, the experimental results of Rullhusen and Schumacher have been plotted in this figure. The differences between our 'exact' RIA calculations and the experimental results are presented at the bottom, and the experimental error bars of Rullhusen and Schumacher are also illustrated in this figure. The differences and the experimental error bars are expressed in percentages.

performed by Bergstrom *et al* [54], and the experimental results are measured by Rullhusen and Schumacher [61]. Furthermore, the differences between our 'exact' RIA calculations and the experimental results, as well as experimental error bars, are presented in percentages at the bottom. The differences between theoretical calculations and experimental results are given by

$$R \equiv \frac{\left(\frac{d\sigma}{d\omega_f d\Omega_f}\right)_{\text{exp}} - \left(\frac{d\sigma}{d\omega_f d\Omega_f}\right)_{\text{theory}}}{\left(\frac{d\sigma}{d\omega_f d\Omega_f}\right)_{\text{theory}}}. \tag{E.1}$$

This figure indicates that the calculated results of our 'exact' RIA treatment and former RIA treatments are in agreement with those of the S-matrix as well as with the experimental results in the Compton peak region. Considering the experimental uncertainties, only small differences exist between our 'exact' RIA calculations and the experimental results. However, both our 'exact' RIA calculations and the former RIA treatments are inconsistent with the S-matrix results outside the Compton peak region, specifically in the cases where the outgoing photon energy ω_f is very low. This could be because of the limitations of RIA formulations, which neglect some interference terms in the dynamical process of Compton scattering and are only a leading order approximation of the more advanced S-matrix formalism [7, 50]. The comparison presented here is consistent with recent studies on Compton scattering, which have indicated that the available ranges for former RIA treatments are near the Compton peak [7, 48–51]. Because of the limited physical picture in RIA formulations, the reliable zones for our 'exact' RIA treatments are still near the Compton peak. Our approach, despite employing exact numerical integration, does not exhibit a significant improvement over the former RIA treatments outside the Compton peak region.

ORCID iDs

Chen-Kai Qiao https://orcid.org/0000-0002-6745-3616

References

[1] Kubo Y 2005 Electron correlation effects on Compton profiles of copper in the GW approximation *J. Phys. Chem. Solids* **66** 2202–6

[2] Pisani C, Itou M, Sakurai Y, Yamaki R, Ito M, Erba A and Maschio L 2011 Evidence of instantaneous electron correlation from Compton profiles of crystalline silicon *Phys. Chem. Chem. Phys.* **13** 933–6

[3] Cooper M J 1971 Compton scattering and electron momentum distributions *Adv. Phys.* **20** 453–91

[4] Cooper M J 1997 Compton scattering and the study of electron momentum density distributions *Radiat. Phys. Chem.* **50** 63–76

[5] Aguiar J C, Mitnik D and Di Rocco H O 2015 Electron momentum density and Compton profile by a semi-empirical approach *J. Phys. Chem. Solids* **83** 64–9

[6] Wang Y J, Lin H, Barbiellini B, Mijnarends P E, Kaprzyk S, Markiewicz R S and Bansil A 2010 Proposal to determine the Fermi-surface topology of a doped iron-based superconductor using bulk-sensitive Fourier-transform Compton scattering *Phys. Rev.* B **81** 092501

[7] Bergstrom P M and Pratt R H 1997 An overview of the theories used in Compton scattering calculations *Radiat. Phys. Chem.* **50** 3–29

[8] Porter T A, Moskalenko I V, Strong A W, Orlando E and Bouchet L 2008 Inverse Compton origin of the hard x-ray and soft gamma-ray emission from the galactic ridge *Astrophys. J* **682** 400–7

[9] Phuoc K T, Corde S, Thaury C, Malka V, Tafzi A, Goddet J P, Shah R C, Sebban S and Rousse A 2012 All-optical Compton gamma-ray source *Nat. Photonics* **6** 308–11

[10] Takada A *et al* 2005 Development of an advanced Compton camera with gaseous TPC and scintillator *Nucl. Instrum. Meth.* A **546** 258–62

[11] Mihailescu L, Vetter K M, Burks M T, Hull E L and Craig W W 2007 SPEIR: a Ge Compton camera *Nucl. Instrum. Meth.* A **570** 89–100

[12] Chiu J-L *et al* 2015 The upcoming balloon campaign of the Compton spectrometer and imager (COSI) *Nucl. Instrum. Meth.* A **784** 359–63

[13] Klein O and Nishina Y 1929 Über die Streuung von Strahlung durch freie Elektronen nach der neuen relativistischen Quantendynamik von Dirac *Z. Phys.* **52** 853–68

[14] Sakurai J J 1967 *Advanced Quantum Mechanics* (New York: Addison-Wesley)

[15] Eisenberger P and Platzman P M 1970 Compton scattering of x rays from bound electrons *Phys. Rev.* A **2** 415–23

[16] Eisenberger P and Reed W A 1974 Relationship of the relativistic Compton cross section to the electron's velocity distribution *Phys. Rev.* B **9** 3237–41

[17] Ribberfors R 1975 Relationship of the relativistic Compton cross section to the momentum distribution of bound electron states *Phys. Rev.* B **12** 2067–74

[18] Ribberfors R 1975 Relationship of the relativistic Compton cross section to the momentum distribution of bound electron states. II. Effects of anisotropy and polarization *Phys. Rev.* B **12** 3136–41

[19] Ribberfors R and Berggren K-F 1982 Incoherent-x-ray-scattering functions and cross sections $(d\sigma/d\Omega)_{incoh}$ by means of a pocket calculator *Phys. Rev.* A **26** 3325–33

[20] Ribberfors R 1983 X-ray incoherent scattering total cross sections and energy-absorption cross sections by means of simple calculation routines *Phys. Rev.* A **27** 3061–70
Ribberfors R 1983 X-ray incoherent scattering total cross sections and energy-absorption cross sections by means of simple calculation routines *Phys. Rev.* A **28** 2551

[21] Gillet J-M, Fluteaux C and Becker P J 1999 Analytical reconstruction of momentum density from directional Compton profiles *Phys. Rev.* B **60** 2345–9

[22] Sahariya J and Ahuja B L 2011 Compton profiles and electronic properties of Nd *Phys. Scr.* **84** 065702

[23] Rathor A, Sharma V, Heda N L, Sharma Y and Ahuja B L 2008 Compton profiles and band structure calculations of IV-VI layered compounds GeS and GeSe *Radiat. Phys. Chem.* **77** 391–400

[24] Brusa D, Stutz G, Riveros J A, Fernbdez-Varea J M and Salvat F 1996 Fast sampling algorithm for the simulation of photon Compton scattering *Nucl. Insrum. Meth.* A **379** 167–75

[25] Salvat F and Fernández-Varea J M 2009 Overview of physical interaction models for photon and electron transport used in Monte Carlo codes *Metrologia* **46** S112–38

[26] Brown J M C, Dimmock M R, Gillam J E and Paganin D M 2014 A low energy bound atomic electron Compton scattering model for Geant4 *Nucl. Instrum. Meth.* B **338** 77–88

[27] LaJohn L A 2010 Low-momentum-transfer nonrelativistic limit of the relativistic impulse approximation expression for Compton-scattering doubly differential cross sections and characterization of their relativistic contributions *Phys. Rev.* A **81** 043404

[28] Grant I P 1961 Relativistic self-consistent fields *Proc. R. Soc. London Ser.* A **262** 555–76

[29] Desclaux J P, Mayersi D F and OB´rien F 1971 Relativistic atomic wave functions *J. Phys. B: At. Mol. Phys.* **4** 631–42

[30] Desclaux J P 1975 A multiconfiguration relativistic Dirac–Fock program *Comput. Phys. Commun.* **9** 31–45

[31] Dyall K G, Grant I P, Johnson C T, Parpia F A and Plummer E P 1989 GRASP: a general-purpose relativistic atomic structure program *Comput. Phys. Commun.* **55** 425–56

[32] Visscher L and Dyall K G 1996 Dirac–Fock atomic electronic structure calculations using different nuclear charge distributions *At. Data and Nucl. Data Tables* **67** 207–24

[33] Undagoitia T M and Rauch L 2015 Dark matter direct-detection experiments *J. Phys. G: Nucl. Part. Phys.* **43** 013001

[34] Liu S K *et al* (CDEX Collaboration) 2017 Constraints on axion couplings from the CDEX-1 experiment at the China Jinping underground laboratory *Phys. Rev.* D **95** 052006

[35] Jiang H *et al* (CDEX Collaboration) 2018 Limits on light weakly interacting massive particles from the first 102.8 kg × day data of the CDEX-10 experiment *Phys. Rev. Lett.* **120** 241301

[36] Agnese R *et al* (SuperCDMS Collaboration) 2018 Results from the super cryogenic dark matter search experiment at Soudan *Phys. Rev. Lett.* **120** 061802

[37] Cui X *et al* (PandaX-II Collaboration) 2017 Dark matter results from 54-Ton-day exposure of PandaX-II experiment *Phys. Rev. Lett.* **119** 181302

[38] Akerib D S *et al* (LUX Collaboration) 2017 Results from a search for dark matter in the complete LUX exposure *Phys. Rev. Lett.* **118** 021303

[39] Aprile E *et al* (XENON Collaboration) 2018 Dark matter search results from a one ton-year exposure of XENON1T *Phys. Rev. Lett.* **121** 111302

[40] Rodejohann W 2012 Neutrinoless double-beta decay and neutrino physics *J. Phys. G: Nucl. Part. Phys.* **39** 124008

[41] Agostini M *et al* (GERDA Collaboration) 2013 Results on neutrinoless double-β decay of ^{76}Ge from phase I of the GERDA experiment *Phys. Rev. Lett.* **111** 122503

[42] Agostini M *et al* (GERDA Collaboration) 2018 Improved limit on neutrinoless double-β decay of ^{76}Ge from GERDA phase II *Phys. Rev. Lett.* **120** 132503
[43] Albert J B *et al* (EXO-200 Collaboration) 2014 Search for Majorana neutrinos with the first two years of EXO-200 data *Nature* **510** 229–34
[44] Gando A *et al* (KamLAND-Zen Collaboration) 2016 Search for Majorana neutrinos near the inverted mass hierarchy region with KamLAND-Zen *Phys. Rev. Lett.* **117** 082503
Gando A *et al* (KamLAND-Zen Collaboration) 2016 Search for Majorana neutrinos near the inverted mass hierarchy region with KamLAND-Zen *Phys. Rev. Lett.* **117** 109903 (erratum)
[45] Barker D and (SuperCDMS Collaboration) 2017 Low energy background spectrum in CDMSlite *Proceedings of Science* 282 874
[46] Ramanathan K *et al* 2017 Measurement of low energy ionization signals from Compton scattering in a charge-coupled device dark matter detector *Phys. Rev.* D **96** 042002
[47] Stutz G E 2014 Compton scattering cross section for inner-shell electrons in the relativistic impulse approximation *Nucl. Instrum. Meth.* B **319** 8–16
[48] Kaliman Z, Pisk K and Pratt R H 2011 Compton scattering from positronium and validity of the impulse approximation *Phys. Rev.* A **83** 053406
[49] Bergstrom P M, Surić T, Pisk K and Pratt R H 1993 Compton scattering of photons from bound electrons: full relativistic independent-particle-approximation calculations *Phys. Rev.* A **48** 1134–62
[50] Pratt R H, LaJohn L A, Florescu V, Surić T, Chatterjee B K and Roy S C 2010 Compton scattering revisited *Radiat. Phys. Chem.* **79** 124–31
[51] Drukarev E G and Mikhailov A I 2016 *High Energy Atomic Physics* (Berlin: Springer) (https://doi.org/10.1007/978-3-319-32736-5)
[52] Biggs F, Mendelsohn L B and Mann J B 1975 Hartree–Fock Compton profiles for the elements *At. Data and Nucl. Data Table* **16** 201–309
[53] Surić T, Bergstrom P M, Pisk K and Pratt R H 1991 Compton scattering of photons by inner-shell electrons *Phys. Rev. Lett.* **67** 189–92
[54] Bergstrom P M, Surić T, Pisk K and Pratt R H 1992 Some preliminary calculations of whole atom Compton scattering of unpolarized photons *Nucl. Insrum. Meth.* B **71** 1–6
[55] Jung M *et al* 1998 Manifestations of nonlocal exchange, correlation, and dynamic effects in x-ray scattering *Phys. Rev. Lett.* **81** 1596–9
[56] Kaplan I G, Barbiellini B and Bansil A 2003 Compton scattering beyond the impulse approximation *Phys. Rev.* B **68** 235104
[57] Surić T 2006 Compton scattering beyond impulse approximation: correlation, nonlocal-exchange and dynamic effects *Radiat. Phys. Chem.* **75** 1646–50
[58] Drukarev E G, Mikhailov A I and Mikhailov I A 2010 Low-energy k-shell Compton scattering *Phys. Rev.* A **82** 023404
[59] Hopersky A N, Nadolinsky A M and Novikov S A 2015 Compton scattering of two x-ray photons by an atom *Phys. Rev.* A **92** 052709
[60] Huang K-N 1980 Theory of angular distribution and spin polarization of photoelectrons *Phys. Rev.* A **22** 223–39
Huang K-N 1982 Theory of angular distribution and spin polarization of photoelectrons *Phys. Rev.* A **26** 3676–8
[61] Rullhusen P and Schumacher M 1976 Cross section profiles for Compton scattering of 279 2 keV photons by copper, tin and lead *J. Phys. B: At. Mol. Phys.* **9** 2435–46